

**Characterization and Determination of Flexible Cardiovascular Biosensors for
Facile Detection of Patient BNP**

by

Seth So

B.S. Electrical Engineering, University of Pittsburgh, 2019

Submitted to the Graduate Faculty of
the Swanson School of Engineering in partial fulfillment
of the requirements for the degree of
Master of Science in Electrical and Computer Engineering

University of Pittsburgh

2021

UNIVERSITY OF PITTSBURGH
SWANSON SCHOOL OF ENGINEERING

This thesis was presented

by

Seth So

It was defended on

March 26, 2021

and approved by

Dr. Minhee Yun, PhD., Associate Professor,

Department of Electrical and Computer Engineering

Dr. Hong Koo Kim, PhD., Professor,

Department of Electrical and Computer Engineering

Dr. Zhi-Hong Mao, PhD., Professor,

Department of Electrical and Computer Engineering

Thesis Advisor: Dr. Minhee Yun, PhD.,

Associate Professor, Department of Electrical and Computer Engineering

Copyright © by Seth So
2021

Characterization and Determination of Flexible Cardiovascular Biosensors for Facile Detection of Patient BNP

Seth So, M.S.

University of Pittsburgh, 2021

The sheer amount of individual patient data can often be inundative. However, filtering through large amounts of data quickly would unlock a powerful key to providing effective and personalized treatments, both proactive and reactive. A great area of interest is improving early diagnosis and management strategies for cardiovascular disease (CVD), the leading cause of death in the world. Treatment is often inhibited by analysis delays, but rapid testing and determination can help increase frequency for real-time monitoring. Thus an improvement to the form factor of collection methods is also needed. In this research, a flexible nano-biosensor was developed and characterized for sensitivity and specificity for single and continuous sampling. Additionally two methods are presented in order to better utilize raw patient data. First, a machine learning (ML) implementation of quadratic discriminant analysis (QDA) was trained on sensor characterization data to develop a model for digital determination. Second, a tunable ultrasensitive bio-signal amplification circuit with a simple LED output was designed for analog determination. Both methods were tested on human blood serum samples from 30 University of Pittsburgh Medical Center patients. The ML algorithm yielded 95% power when separating samples, comparable to 3-dimensional principal component analysis (PCA) results. The circuit was able to accurately identify each sample as one of three categories: sub-threshold, analog, and saturation regions, corresponding to $0 < [C] < 500$ pg/mL (LED_{off}), $500 < [C] < 1000$ pg/mL (LED_{dim}), and 1000 pg/mL $< [C]$ (LED_{bright}).

Keywords: biosensor, BNP, cardiovascular, LED, ISFET, nanomaterial, point-of-care.

Table of Contents

Preface	x
1.0 Introduction	1
2.0 Preparations	6
2.1 Materials	6
2.1.1 Chemicals and Reagents	6
2.1.2 Circuitry and Development	6
2.2 Work Environments	6
3.0 Biosensor Fabrication	7
3.1 Wafer Processing	7
3.2 PANI Growth	9
3.3 Surface Modification	10
3.4 Sensor Overview	11
3.4.1 CAD Model	11
3.4.2 Theory of Operation	11
3.4.2.1 Sensing Principle	11
3.4.2.2 Detection Range	13
3.4.2.3 BSA Blocking	14
3.4.3 Topology Effect	15
4.0 Sensor Characterization	17
4.1 Electrical Measurement	17
4.2 Test Sample Types	18
4.2.1 Artificial Samples	18
4.2.2 Human Samples	18
4.3 Single Sample Tests	19
4.3.1 Spiked PBS Samples	19
4.3.2 UPMC Patient Serum (Healthy)	21

4.3.3 UPMC Patient Serum (Unhealthy)	22
4.3.4 Hemolysis Impact	23
4.4 Multi Sample Tests	25
4.4.1 Continuous Spiking	25
4.4.2 Biomarker Specificity	26
4.4.3 Reaction Reversability	27
5.0 Determination Methods	29
5.1 Digital Determination - Machine Learning Analysis	29
5.1.1 Discriminant Analysis	30
5.1.2 Principal Component Analysis	32
5.2 Analog Determination - Readout Circuit	33
5.2.1 Circuit Operation	33
5.2.2 Noise Reduction	34
5.2.3 Optical Output States	34
5.2.4 System V-I Characterization	36
6.0 Conclusion	38
Appendix A. Example Sweep Data	39
Appendix B. Chipset Data Sheets	41
Bibliography	43

List of Figures

1	4 in. PET wafer cut-out and cleaned, with flexibility demonstrated	7
2	Wafer with gold electrodes deposited, forming a 5x5 array of 6 sensor cells, sharing common sources and drains	8
3	(Left) PANI synthesized directly onto wafer; (Right) closeup of PANI grown on exposed electrode bridge	9
4	Closeup of crosslinker-antibody solution pipetted directly onto PANI film layer. Chamber humidity was controlled to ensure the solution did not evaporate during the 6 hour window	10
5	CAD rendering of biosensor in operation: Au/Cr electrodes on PET wafer with mAb-functionalized PANI bridge. A drop of human blood serum with BNP is placed directly on top of the functionalized area. Sample antigens bind to the antibodies, causing a charge accumulation biasing the PANI layer and increasing conductivity	11
6	(Left) Incomplete conformation results in reduced PANI conductivity; (Right) Higher antibody-antigen binding results in increased PANI conductivity	12
7	Strength of ionic solution is inversely proportional to Debye screen length, such that higher strength results in a reduced sensing radius	14
8	BSA molecules block space otherwise occupied by charged non-targets that may affect the output signal	14
9	(Left) Labelled image of custom built test rig; (Right) close-up of gold contact headers	17
10	Current response results from spike testing experiment for PBS, control sample, 200, 400, 800, 1000, 2000, and 3000 pg/mL. Linearly increasing current responses demonstrate proper function of the biosensor. Gate voltage is -0.4V due to p-type nature of PANI and prior testing	20

11	Current responses for 100 baseline (healthy patient blood samples) tests across 10 samples. Each test has 80 points taken during a linear sweep from [0 - 0.4] V. Results are plotted to form a heatmap – darker regions indicated higher density of results among multiple samples and lighter regions indicate more sparse measurements	21
12	Variance plot organized according to devices that each measurement was taken from. Data characterizes range of current responses of healthy samples. Maximum intra-device range was 1nA, indicating good replicability and reliability to not in higher ranges	22
13	Blind test current responses were color coded according to concentration (control 1, control 2, 600, 800, and 1800 pg/mL). and confusion matrix. Results show clear separation between healthy patients and those with high levels of BNP in blood. As BNP concentration was increased, variance increased significantly at higher gate voltage. Clear separation was achieved between blood samples with trace amounts of BNP and patients with at-risk levels of BNP	23
14	Heat map plot of hemolysis current magnitude sweeps. Green corresponds to lower response, and red corresponds to higher response. The total range in testing is 4 pA, indicating that while there is an inverse relation between hemoglobin concentration and conductivity, the overall effect is quite minimal	24
15	Concentration dependency of increasing levels of BNP (25, 100, 250, 750, 1200 pg/mL). For each application, current magnitude increases in agreement with prior characterization. Bulk reactions take several seconds to reach equilibrium, and appear to occur at a linear rate due to low sampling rate	25
16	Specificity towards target BNP vs non-target biomarkers. Application of each nontarget biomarker affects current response with less than 10% of BNP sensitivity. The final BNP sample confirms proper sensor function	27

17	Specificity test with additional intermediate PBS0.1x washing steps to gauge reaction affinities. Washing procedure consisted of 3 rounds of PBS dilution and removal through pipetting. Results indicate that most non target biomarkers are physically bound to the PANI layer, but the BNP antigen-antibody complex is not washed away during the purging, showing high affinity relative to blocked biomarkers	28
18	Confusion matrix of classifier results were used to calculate power and error. All results were comparable to standard methods such as PCA. Metrics derived from the matrix are: accuracy (95.2%), sensitivity (97.6%), specificity (92.9%), precision (93%), and recall (98%)	31
19	3d-PCA analysis of blind test samples. Components were mean current, current variance, and mean charge. Blue indicates samples classified as healthy and orange indicates samples classified as unhealthy	32
20	High level block schematic of system. 3 stages are: 1. Current generation through antigen sensing, 2. Transimpedance amplification for voltage control, and 3. Final voltage inversion and amplification	33
21	LED states with corresponding visuals. Concentrations applied in order were: 25, 100, 250 (State 0 – LED _{off}), 750 (State 1 – LED _{dim}), and 1200 pg/mL (State 2 – LED _{bright}). Gain was tuned for concentration threshold of 500 pg/mL between State 0 and State 1	35
22	V-I characteristic of system mirrors that of LED, formed by plotting induced sensor current versus output LED voltage. ISFET generates a negative current but the signal voltage is inverted during amplification, resulting in a reflected. Additionally, note that in this circuit operation, LED voltage is a function of sensor current, opposite of standard I-V characteristic convention. Characterization matches expectations and validates holistic circuit design	37
23	Raw current data from five tests of a serum sample with low BNP	39
24	Raw current data from five tests of a serum sample with high BNP	40
25	AD8484 general description	41
26	TLE207x general description	42

Preface

I would like to extend my sincere gratitude to Dr. Minhee Yun, my research advisor, for your guidance throughout my time as both an undergraduate and graduate student at the University of Pittsburgh. Without you, I would likely never have gotten involved in the research space, a crucial experience to both my academic and personal growth. Thank you for the support over the past three years!

I would also like to extend thanks to the entire SSoE ECE faculty. From industrial scale applications to nanoelectronics to computer vision, every course offered was truly enriching and enjoyable. Your passion for electrical engineering clearly shone through your teaching, and now it will continue on with me.

To the ECE department administrative staff, especially Sandy and Nicole, thank you for answering my endless barrage of questions. Without you, I would still probably be a clueless undergraduate, unknowingly missing some gen-ed required for graduation.

To my fellow peers, they say shared experiences are the core of every meaningful relationship. Here's to staying life-long friends.

Finally, a special thanks to my parents. Mom and Dad, my most valuable takeaway from university has been growing up for the past 4.5 years. Thanks for letting me take my time with that, I know you will always be there for me.

1.0 Introduction

Modern day biosensing technology is approaching an inflection point from research to clinical use. As a technology, biosensors are no longer in their infancy and are beginning to make large strides almost daily in both performance and understanding of mechanism. Due to the adaptation of existing nanofabrication techniques and infrastructure used for modern day electronics, new biosensing methodologies and morphologies are becoming more complex and varied without sacrificing precision. This presents exciting opportunities for new applications and inquiries.

Over the past decade, conductometric sensors have been significantly developed [1, 2, 3]. This sensing methodology has well established its broad range of capabilities and greatly expanded the repertoire of biosensors as a whole. Due to mechanistic advantages in sensitivity and specificity especially, conductometric biosensors have become of particular use in a plethora of biosensing applications. A major area of study currently is the detection of pathogens through the use of functionalized electrodes [4]. The method is to modulate the conductivity of an electrode bridge using either primary or secondary binding sites that accumulate or disperse charge in the presence of target molecules. Such a method can be easily accomplished with conjugate molecules, but utilizing coupling complexes to indirectly entrap targets inherently introduces significant specificity to the sensing. Recently, this has been accomplished with bacterial entrapment for the detection of phenol, an environmentally corrosive by pollutant [5]. Researchers were able to immobilize a strain of bacteria onto gold electrodes in order to detect down to 0.2 mg/L of phenol, and they are in contention for making the first conductometric sensor to sense the compound. The method of indirect sensing creates potential to detect nearly any biological target with precision and accuracy, so long as there exists a target-coupling complex. One of the most studied topics is the use of antibodies since they provide great affinities with their associated antigens. Researchers from the University of Lyon demonstrated detection of the protein creatinine through entrapment of its metabolic enzyme, creatine deaminase in a biosensor [6]. They were able to achieve down to 2 μM sensitivity and an ultimate range of [10 - 600] μM range with strong

repeatability. There is still a long path left improving conductometric sensors; however, their inherent advantages over current biosensing methodologies in essentials like sensitivity, size, and response time, display great promise in achieving the end goal of clinical use.

Current biosensing methodologies can be very powerful, but they lack in several key practical characteristics that reduce usability. First there is often a slow response time – methods like mass or flow cytometry operate on a per cell basis. This enables great analysis depth, but the process is bottlenecked by sample size. The machines required to do this are also often expensive and large, unable to be housed in the hospitals themselves. As such, the machines, as powerful as they are, are often housed in specialized third party laboratories – the logistics of which introduce multiple potential failure points as well as weeks of lead time. There is also a trend of increasing complexity for other biosensors and established methods. In order to compensate for perceived shortcomings, auxiliary systems are being introduced.

A great deal of work has been done on augmenting biosensors with these systems. An international collaboration between Harvard, the Massachusetts Institute of Technology, Technical University Munich, and Institute for Basic Science (IBS) in Seoul garnered attention after creating a new architecture to greatly improve their heteronuclear magnetic resonance (NMR) biosensor [7]. NMR systems have become a standard and are widely used for their powerful resolutions, but they suffer from long assay times and single channel detection. This issue of limited throughput often bottlenecks different procedures, affecting the technologies usefulness. The team aimed to fix this problem by digitizing much of the hardware and adding multi-channel detection capabilities. Doing so greatly increases throughput and versatility, while also decreasing complexity and cost. The system, HERMES (heteronuclear resonance multichannel electronic system), was tested for application in dengue fever detection and cancer cell profiling to prove successful realization. Aside from technical advancements, improvements to form factor are also a popular topic. Other works include creating much more integrated solutions into portable, handheld packages. Researchers from Greece created a capacitive sensor readout circuit for non-destructive analysis [8]. The circuit fully digitizes capacitance readings to femto regime resolution, and sends the information through USB and R232 connections for extremely high-speed sensing. Similarly, researchers from Germany and Vietnam made a miniaturized readout circuit for variable ion-selective field

affect transistor (ISFET) arrays, along with LabVIEW software for a comprehensive analysis of results, all housed in a case just inches in length [9]. While these are all fantastic works in increasing the power or portability and usability of biosensor systems, there can be many improvements made to reduce to the complexity of the system even further, such as removal of processing units. For biosensors to be more useful in point-of-care settings, they need to be smaller, maintain high standards of sensitivity and specificity, and above also face improvements in form-factor.

These are all areas where conductometric biosensors offer advantages. The simplistic sensing mechanism only requires two electrodes and a bridge. This enables a 2-dimensional topology suitable for both miniaturization and mass production. Consequently, operating procedure is also extremely simple, and output signals are single parameters that are easily interpreted. Bridge topology can be modified at the nano-level, through limitless surface textures (gratings, digitization, etc...) or functionalization (nanoparticles, carbon nanotubes, graphene, antibodies, etc...), in order to improve sensitivity and specificity measurements [10 – 15]. At certain stages of the clinical process, it is desirable to have as low complexity systems as possible. For instance, large scale batch testing requires high throughput, so any non-scalable design can dramatically slow down the process. Aside from time, in diagnostic scenarios, cost is also an important consideration. Biological reagents can often be extremely costly, so mismanagement of resources could lead to shortages. While high power machines have their uses, conductometric sensors offer to fill the void in triage-capacity devices for time-sensitive and high-risk applications, such as cardiovascular diagnosis.

Cardiovascular disease (CVD) has the extremely high prevalence and is the leading cause of global mortality [16 – 18]. In pathologies like myocardial infarction where the ventricles undergo strain, the biomarker B-type natriuretic peptide (BNP) is released, and as such has proven to be an excellent indicator for CVDs [19 – 21]. However, due to expensive testing and long result wait times, regular cardiovascular health testing has yet to be adopted as a standard practice, even though common indicators like BNP and cholesterol are known causes. Biosensors are becoming more viable options in order to change this and enable easier cardiovascular health monitoring. Recently a group from China pushed the bounds of cholesterol detection with a novel gold nanoparticle sensing system [22]. The system achieved

a low limit of 2nM with a signal to noise ratio (SNR) of 3 and displayed linear characterization from 0.0004 to 15.36 mM ($R^2 = 0.9986$), a range well-suited for early diagnosis of heart disease. In order to encourage regular testing and thereby mitigating overall risk of chronic CVDs, biosensor systems need to be usable, focusing on simplicity, speed, and diagnosis. Doing so will be a formative step in making biosensors a mainstay of modern medical clinical technology, and small sensor applications are being developed towards better point-of-care options with advantages in price, efficacy, form factor, and usability [23 – 28].

With better base characteristics and higher standards for biosensors, new facets of biosensors are being explored that can increase utility, such as use of new data assessment methods for characterization and use of flexible substrates for wearable sensors. This is an advantage that electrical sensors hold over other types. They can be used in dynamic working environments, because they depend primarily on conductivity of electrodes, while methods like optical are extremely susceptible to external noise. Standard fabrication techniques can also be used to make biosensors on flexible substrates instead of harder substrates like silicon. In conjunction, these sensors are able to maintain much of the same capabilities of normal sensors but are much more suited to being used in dynamic environments due to their ability to stretch and bend while retaining function.

When fabricated on a flexible substrate, sensors become even more versatile as they have the advantage of being comparatively light while maintaining mechanical strength. Additionally, they can be very thin, which when paired with flexibility, makes flexible substrates very robust and non-brittle. Economically, polymers and plastics are much more affordable but can also have a wide range of physical capabilities. Flexible substrates' potential to be useful in low-cost, dynamic environments make them standout options for a myriad of niche applications such as shear-normal hybrid stress sensors [29], conductive skins for tactile robotics applications, and even liquid-filled membranes for microfluidic-based sensing. Flexibles have an especially strong future in medical context for both in-situ and in-vivo applications. Recently, transparent polymers like polyethylene terephthalate (PET) have been growing in use for biosensors as a substrate for patterning electrodes and growing cells for biosensors. These devices allow for a real-time monitoring, can provide instant feedback, and have predictive warning capabilities. They offer strong resolution and reliability for their

price along with accessibility in daily life. A unique aspect of wearable biosensors is that they are most often noninvasive, gathering different solutions from less commonly analyzed but ubiquitous biofluids like sweat and saliva [30, 31]. Aside from physical benefits, wearables can often have mental effects as well. Having easily accessible information can help an individual make more informed lifestyle choices and serve as steadfast reminders throughout the day, encouraging user engagement [32]. Many different types of wearable sensors have been developed for a wide array of purposes. Some take the form of patches, and most recent commercial options involve wrist watches. Other nontraditional forms of wearables are being explored, such as contact-lens glucose sensors and tattoo-like perspiration monitors. Regardless of form, wearable sensors have been successfully developed for many purposes ranging from blood glucose [33] for glycemia monitoring to perspiration [34] for metabolic analysis and have demonstrated feasibility in many of use cases.

In this research, an ISFET biosensor was developed using modern nanofabrication techniques to allow for higher specificity, portability, and reproducibility. PET, a low-cost and flexible polymer material, was used as the substrate so that the sensors were light and robust for dynamic environments like being worn by a patient. In order to help with diagnosis of HF, the biosensor was modified for the detection of BNP using monoclonal antibodies on a PANI growth template. For determination, two methods were explored. First, an analog determination method is presented as a hardware solution for direct biosignal amplification to an LED, resulting in three state categorization. Second, a digital determination method is presented in a software solution through machine learning classification algorithm developed to classify the immunoassay-based patient readings into two categories, healthy or at-risk. Both methods are system prototypes for making a lab-on-a-chip wearable sensor to allow for regular BNP monitoring. Signals were generated from both artificial samples and real patient blood from University of Pittsburgh Medical Center Patients.

2.0 Preparations

2.1 Materials

2.1.1 Chemicals and Reagents

Acetone, IPA, DI water, N₂ gas, LOR-b photoresist, SC1827, Chromium, Gold, 351 and AZK developer were all used from clean room facility's stock. Aniline [$C_6H_5NH_2$], Ammonium persulfate [$(NH_4)_2S_2O_8$], Perchloric acid [$HClO_4$], EDC [$C_8H_{17}N_3$], NHS [$C_4H_5NO_3$], and bovine serum albumin (BSA) were purchased from Sigma Aldrich. Mouse anti-BNP and recombinant Human BNP were purchased from Novus Biologicals. All dilutions were made with 0.01x PBS.

2.1.2 Circuitry and Development

Chipsets include AD8428 instrumentation amplifiers and TLE207X Excalibur JFET-input op-amp. All components including resistors (gold-band) and capacitors (ceramic) were acquired from Mouser Electronics. Standard perfboard was used for final soldermounting. Simulations and calculations were conducted with LTSpice and MATLAB.

2.2 Work Environments

Research work took place in four main locations. All wafer processing was conducted in the Gertrude E. & John M. Petersen Institute of Nanoscience and Engineering Nanoscale Fabrication and Characterization Facility (NFCF), an ISO-4 grade clean room located in the University sub-basement. Wafer modifications and testing took place in a biohazard-safe lab space in a certified fumehood. Circuit prototyping and construction took place in the Student Electronics Resource Center (SERC), and analysis was carried out in the Nanoelectronics and Devices Laboratory (NEDL) group space.

3.0 Biosensor Fabrication

3.1 Wafer Processing

A sheet of PET was cut into the shape of a 4 in. wafer and cleaned with acetone for 5 minutes followed by a bath in isopropyl alcohol for 3 minutes to remove the acetone (Fig. 1) Excess isopropyl alcohol was evaporated with inert nitrogen gas. This cleaning process and all subsequent work took place in a clean room fume hood to decrease risk of contamination. After cleaning, the PET wafer was wet mounted to a silicon wafer by pipetting several drops of deionized (DI) water onto the silicon wafer before gently putting the PET wafer on top. The wet mount provided enough adhesion and a rigid body that would enable the PET wafer to be spin-coated with Laurell spinners. First, a layer of LOR-b (lift-off resist-b), a photoresist optimized for metal ion developers, was spin coated on at 3000 rpm for 45 seconds, then baked at 115 °C for 2 minutes. After the first minute, a preheated silicon wafer was placed directly on top of the PET wafer to complete baking. Second, photoresist SC1827, a positive resist optimized for g-line exposure, was spin-coated on at 4500 rpm for 45 seconds to adjust for viscosity. The PET was hard baked following the same baking procedure, but the preheated silicon wafer was held steady to hover above the PET wafer without making contact to even the baking process while avoiding any undesired sticking between the two.

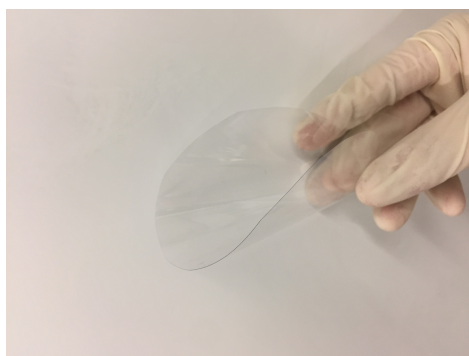


Figure 1: 4 in. PET wafer cut-out and cleaned, with flexibility demonstrated

The MLA100 from Heidelberg Instruments, a liquid crystal maskless laser aligner, was used to expose an electrode pattern designed in AutoCAD, at a dose of 240 mW/cm^2 , found in previous dosage tests. The wafer was then developed in a 1:4 solution of AZK400, a developer complimentary to the LOR-b resist used earlier. The wafer was observed under an infrared microscope to check for proper exposure. Next, 80 nm of gold and 5 nm of platinum were deposited on via electron deposition by a Plassys machine. Gold was chosen for its high conductivity and resistance to oxidation, and the small amount a platinum was added to increase elasticity without greatly affecting conductivity. Lift-off was performed with 1165 remover to dissolve the remaining resist and any metal not directly deposited onto the PET wafer due to the bilayer photoresist. With the electrodes deposited, the wafer was ready for PANI growth to bridge the electrodes (Fig. 2).

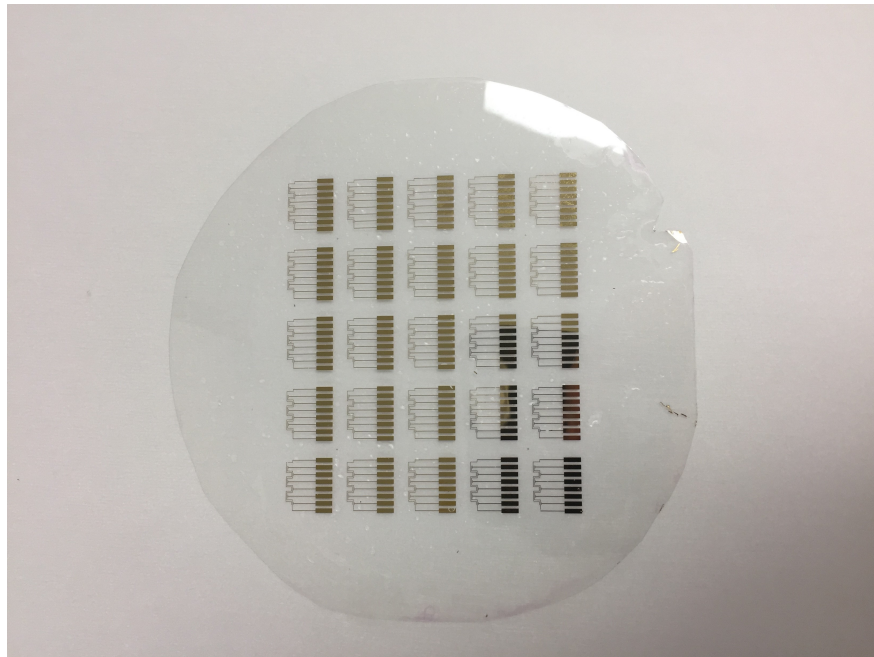


Figure 2: Wafer with gold electrodes deposited, forming a 5x5 array of 6 sensor cells, sharing common sources and drains

3.2 PANI Growth

The same lithography process was used to create an exposed area bridging the electrodes onto which polyaniline (PANI) was chemically synthesized. PANI is an intrinsically conductive organic polymer that is known for its low ionization potential and high electron affinity. PANI was used here as a p-type semiconductor that was capable of entrapping other biological molecules. The PET wafer with gold-platinum electrodes was submerged in a beaker of 200 mL deionized water ($> 13G\Omega$). This beaker was set in an icebath to slow the growth rate for more precise film synthesis. The water was protonated with 6mL of perchloric to control the pH of the solution and avoid unwanted products. 911 μg of aniline was slowly mixed in, followed by 700 mg of aqueous ammonium per sulfate (APS), which acted as the oxidant. The solution was left to stir at 300 rpm via stir bar in the dark in order to promote polymerization of aniline monomer nucleation sites. After 90 minutes, the wafer was removed and dried with nitrogen to leave the aniline in a half-oxidized state and prevent over emeraldization for optimized performance. After growth, any PANI not chemically adhered to the exposed electrodes or PET was washed off in an acetone bath for 5 minutes before being rinsed with water (Fig. 3).

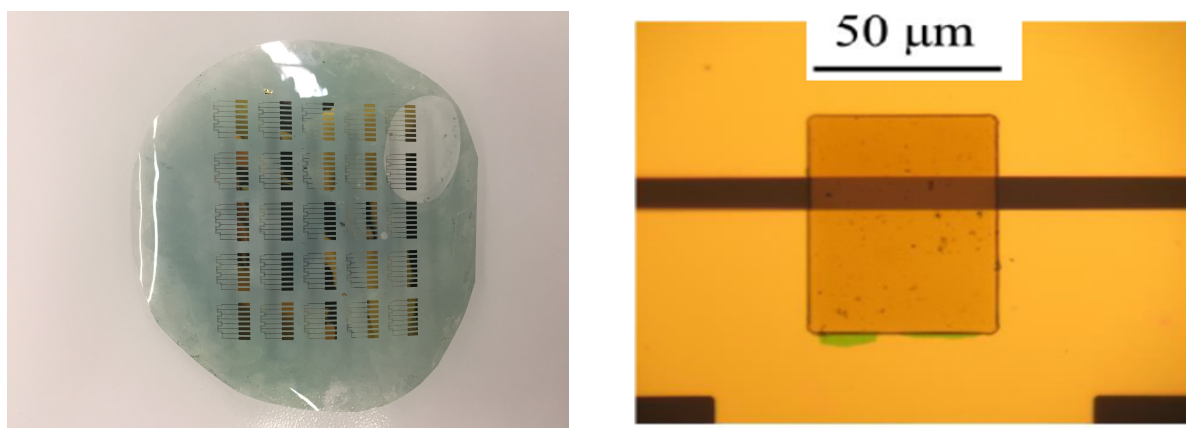


Figure 3: (Left) PANI synthesized directly onto wafer; (Right) closeup of PANI grown on exposed electrode bridge

3.3 Surface Modification

Because PANI and BNP-monoclonal antibodies (mAb) cannot directly bind, surface modification was achieved by using 1-ethyl-3-(3-dimethylaminoprppyl) carbodiimide (EDC) as a crosslinker to bind PANI on one terminal and the antibodies on the other terminal. N-Hydroxysuccinimide (NHS) was added to accelerate the crosslinking process. A uniform solution of antibody, EDC, and NHS was prepared in a 2:49:49 ratio, and the 2.5 μL of this solution was pipetted onto each device and left to adhere to the PANI for 6 hours (Fig. 4). Another 2.5 μL of 20 ng/mL reconstituted lyophilized bovine serum albumin (BSA) powder was pipetted onto each device 30 minutes prior to testing in order to prevent non-specific binding. Devices were tested immediately after in order to prevent antibody variation.

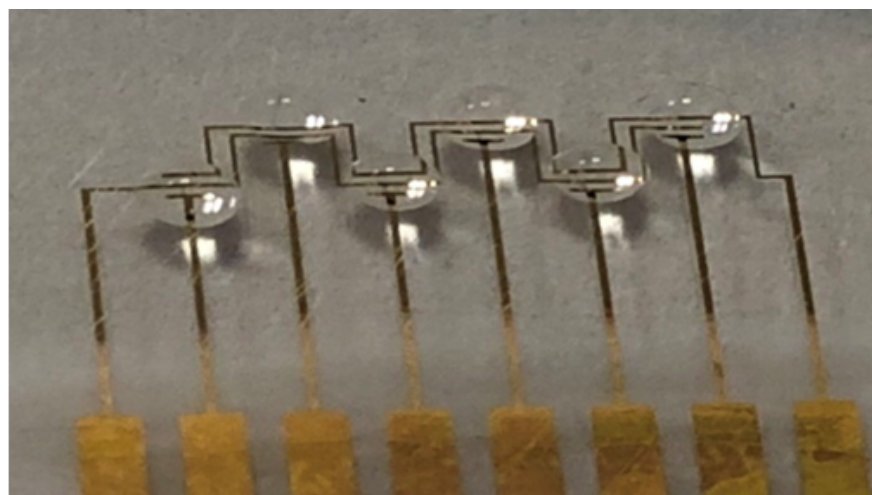


Figure 4: Closeup of crosslinker-antibody solution pipetted directly onto PANI film layer. Chamber humidity was controlled to ensure the solution did not evaporate during the 6 hour window

3.4 Sensor Overview

3.4.1 CAD Model

The resulting device is shown below (Fig. 5). The primary substrate is a sheet of PET that is translucent and able to flex. On top are conductive gold electrodes deposited with a small amount of platinum for added structural support. A thin sheet of PANI bridges the two electrodes and serves as the binding site for the mAb. A droplet of serum is then deposited onto the device, and any sample BNP binds to the receptor side of the mAb, inducing a change in gate voltage.

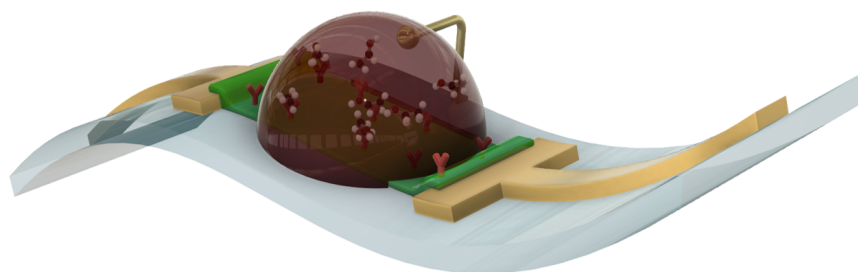


Figure 5: CAD rendering of biosensor in operation: Au/Cr electrodes on PET wafer with mAb-functionalized PANI bridge. A drop of human blood serum with BNP is placed directly on top of the functionalized area. Sample antigens bind to the antibodies, causing a charge accumulation biasing the PANI layer and increasing conductivity

3.4.2 Theory of Operation

3.4.2.1 Sensing Principle

From a chemical perspective, the device operates via well-known biological effects. Antibodies are proteins that act as receptor molecules that only recognize one (monoclonal) or several (polyclonal) specific other molecules, the antigen. Only specific sites found on the target antigen are able to chemically bind to the antibody, which has complex folds to

prevent nonspecific binding. This antibody-antigen interaction is utilized in capturing the BNP molecules found in human blood with mouse monoclonal antibodies. Because BNP is a negatively charged protein, the number of molecules that bind can be used as a dial to control the resistivity of the device, and hence how much electrical current is able to flow through.

From an electrical perspective, the sensor utilizes a 2-dimensional nano PANI sheet – a semiconducting organic polymer, to which anti-BNP is cross linked. When a droplet of blood is deposited onto this sheet, the BNP will bind to its high-affinity receptor molecule. Because BNP is a negatively charged peptide, this binding will create a sheathe of negative charge above the PANI surface, which in turn induces a positive voltage on the PANI (Fig. 6). Due to its semiconducting properties, the magnitude of this voltage is directly proportional with its electrical conductance. A voltage is applied to the two electrodes on either side of the PANI bridge to see the resulting current – this current can be used to infer the amount of charge built up on the surface of the PANI, and hence how many molecules have bound and are in the blood. This is the core operating principle of ISFETs, which were first used to great success for counting H^+ ions to deduce pH levels.

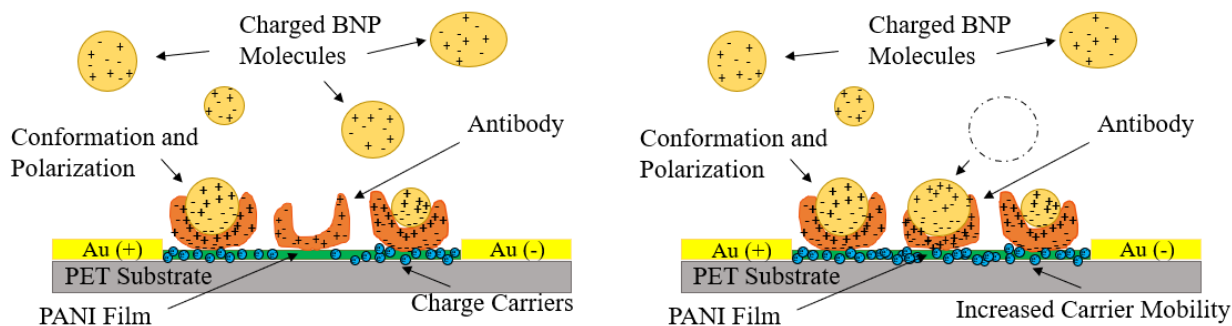


Figure 6: (Left) Incomplete conformation results in reduced PANI conductivity; (Right) Higher antibody-antigen binding results in increased PANI conductivity

3.4.2.2 Detection Range

The limit of detection and specificity are dependent on the dimensions of the PANI sheet, smoothness of substrate surface, and antibody concentration. This equation was used to calculate the effective spatial range of detection, or Debye length:

$$\lambda_D = \sqrt{\frac{\epsilon_0 \epsilon_r k_B T}{\sum (\rho_i z_i)^2}} \quad (3.1)$$

Where ϵ_0 and ϵ_r are the dielectric constant of vacuum and relative permittivity, k_B and T are the Boltzmann's constant and the temperature in Kelvin, and ρ_i and z_i are the density and the valence of the i -th ionic species. The equation can be further simplified when at room temperature (25 °C):

$$\lambda_D = \frac{2.15e(-10)}{\sqrt{I_s}} \quad (3.2)$$

I_s represents the ionic strength of the solution. This corresponds to a Debye length $\lambda_D = 0.7\text{nm}$, 2.3nm , and 7.3nm for PBS solutions of 1X, 0.1X, and 0.01X respectively (Fig. 7). PET has a rougher surface structure than standard metal oxide wafers, which results in a greater surface area of synthesized PANI. This leads to more binding sites for antibodies, raising the upper limit of antigen detection. Additionally, surface roughness increases the Debye sphere volume, screening out far less site bindings, increasing efficiency of the system. Overall an ionic solution of PBS 0.01X should result in ISFET detection limits to a floor of 50pg/mL and a ceiling of 2000 pg/mL, which sufficiently encompasses the BNP range of interest.

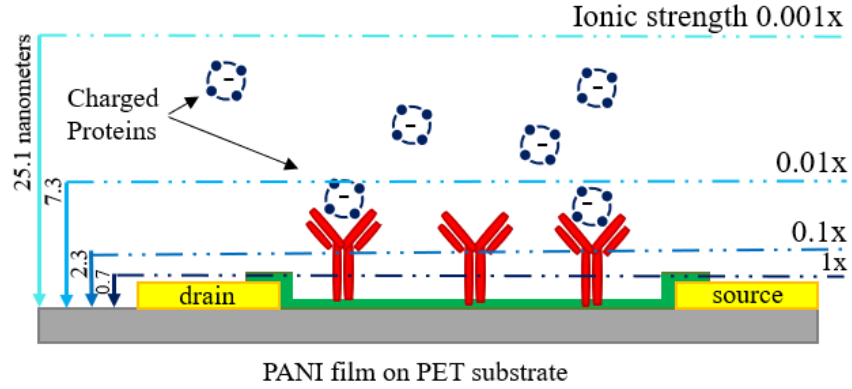


Figure 7: Strength of ionic solution is inversely proportional to Debye screen length, such that higher strength results in a reduced sensing radius

3.4.2.3 BSA Blocking

As mentioned before, the final step before testing is BSA blocking, which is a technique to minimize non-specific binding. The BSA molecules act as an insulating carpet, covering exposed PANI space that other biomarkers could physically adhere to. Doing so shifts the effective Debye screening region to only where BNP molecules are located, greatly increasing the ratio of targets to non-targets and hence the signal to noise ratio (Fig. 8).

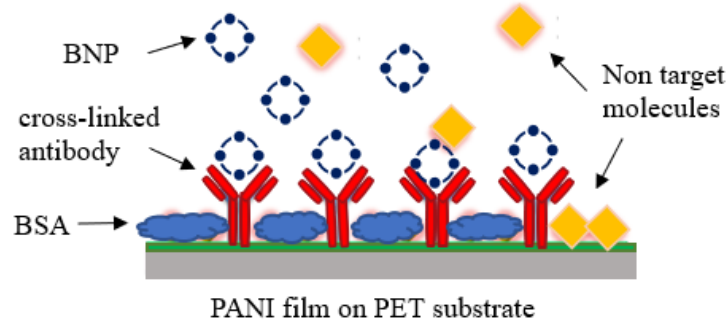


Figure 8: BSA molecules block space otherwise occupied by charged non-targets that may affect the output signal

3.4.3 Topology Effect

The topology of the sensor should result in several predictable characteristics present in the output signal waveform. In particular, one of the primary advantages of using nanosensors is the increased sensitivity. This is due to the square-cube law, which dictates that as surface area and volume are inversely proportional. As mentioned previously, PET has a rougher surface, resulting in a textured PANI layer where binding sites are packed more tightly. However, decreasing dimension to maximize surface area comes with a caveat - there is a tradeoff between input signal sensitivity and output signal stability.

The loss of signal stability comes from several sources. From a mathematical viewpoint, smaller signals are relatively closer in magnitude to any noise introduced by the system. This will inherently drive the signal to noise ratio (SNR) lower unless noise is controlled. Secondly from a chemical perspective, as fewer reactions are occurring, the granularity of the law of mass action begins to become evident. Reaction equilibrium becomes more difficult to achieve, and the output signal shifts from a static average to a moving average. Physical effects are also at play when decreasing dimensions. As more binding are readily available, some sensing reactions can cause additional losses. A study utilizing palladium nanowires to detect trace hydrogen gases posited that the reaction caused continual opening and closing of "break junctions," or micropores within the nanowires [35]. These repetitive reactions greatly increase mass hysteretic effects, which destabilizes the signal. Thus if there are noise control limitations, a proper balance with size must be conditioned.

Therefore for this research, a 2-d topology was chosen despite capabilities for 1-d nanowire growth. Choosing a larger surface area better fit the desired target detection ranges, while also guaranteeing a more stabilized output signal. This design choice should ensure high SNR and allow for smooth curves unaffected by noise, an important design consideration for reliability.

Low signal noise is essential for high sensitivity applications. In this research, this matters for both methods of determination, later discussed in more detail. First, clean data directly affects the efficacy of post-collection analysis. In the case of complex machine learning algorithms, minimizing SNR is often what determines whether or not it will be able

to output decisions with any accuracy at all. The type of data collected in this research makes the issue even more imperative. Each measurement consists of at minimum eighty sub-measurements, such that noise affecting individual points would cumulatively affect the quality of the sweep. As the algorithm requires as much training data as possible, the effect of noise is amplified even further. Therefore in order for best separation and performance, input data needs to be as denoised as possible.

The second method of output determination is through direct bio-signal amplification. In this instance, the importance of a high signal to noise ratio is much more clear. Because input current is being measured on the nanoampere regime, any amount of noise inherent to the collection process will greatly affect the signal. Here, SNR takes on a much more concrete meaning, as physical gaussian noise superimposed onto the actual current response will account for a greater relative component of the total signal when noise is high. Thus during amplification, SNR needs to be held at a minimum in order to minimize the amount of noise that is amplified. This also has advantages for circuit design. When there is low input noise, system gain can be front-loaded. As a result, noise injected at subsequent stages of amplification are not boosted as much. Therefore components with low noise are less important, and other performance characteristics such as bandwidth can be prioritized.

In either case, sensor morphology can be viewed from a system process point of view. Choosing a 2-d sensing layer is a preprocessing step that ensures the quality of the output signal, either before or after subsequent processing. Compared to a 1-d nanowire, the 2-d sheet resulted in a much smoother, stabler signal. The sensitivity tradeoff can easily be made, prior testing has confirmed that the BNP range of interest is already well encompassed as the limit of detection for the 2-d PANI sheet is sufficient for the purposes intended.

4.0 Sensor Characterization

4.1 Electrical Measurement

Below is an image showing the measurement and characterization set up for the biosensors fabricated in this research (Fig. 9). The biosensors are on clear, flexible substrate, sitting on a controllable stage. Devices were vacuum-mounted onto on a 3-axis stage (x, y, θ). To the right is a close-up showing how the probe contacts the device during testing. The $2 \mu\text{L}$ droplets of control serum can be seen on the PANI sheet bridging the electrodes. After surface modification and BSA blocking, a motorized 6 channel copper probe was lowered onto the gold contacts for electrical connection, and optimized gate voltage of -0.4 V was applied with an external power source from Rigol Technologies. Devices were then tested with linear sweep voltammetry using a potentiostat from CH Instruments.

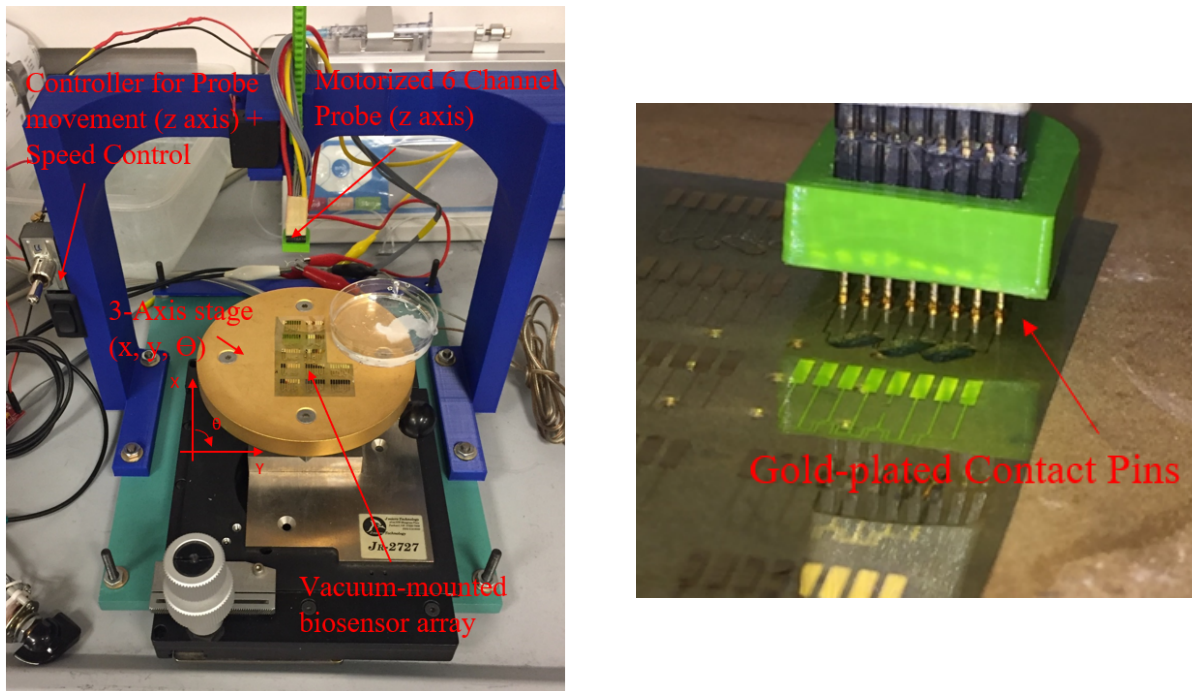


Figure 9: (Left) Labelled image of custom built test rig; (Right) close-up of gold contact headers

For single sample testing, a voltage sweep was run from [0 - 0.4] V, measurements were taken every 5 ms, and sensitivity was set to nanoampere scale. A single sample was measured at a time, and the current response and reference charge were locally recorded using the same instrument. For multi sample tests, a constant voltage of 0.4V was applied and the current response was again recorded, this time with a sampling rate of 1 sample per second to accommodate for longer test times. In these tests, difference sequences of biomarkers were pipetted onto the sensor at predefined time intervals.

4.2 Test Sample Types

4.2.1 Artificial Samples

For characterization baseline and comparison, several artificially spike samples were prepared throughout the course of testing. This included various PBS0 0.01x dilutions of recombinant human BNP in varying amounts, and additional cardiac biomarkers hemoglobin, myoglobin, creatine-kinase (CK), and c-troponin (CTNI) in natural amounts. Samples were kept in mini aliquot tubes and refreshed every 2 months, minimizing stock freeze-thaw cycles.

4.2.2 Human Samples

Deidentified samples from healthy controls and patients with CVD were obtained from an ongoing heart failure registry at the University of Pittsburgh. The protocol was approved by the Institutional Review Board, and all subjects provided informed consent and chose to remain fully anonymous. Venous blood was collected using Vacutainer serum tube, and blood samples were kept at room temperature for 30 minutes and centrifuged at 1500 xg for 15 minutes in a table-top centrifuge. Doing so separated larger molecules from the sample such as hemoglobin and platelets to reduce contaminant noise and increase signal to noise ratio. Serum samples were collected and stored in 20 μ L aliquots at -80 °C. Each aliquot was tested and labelled for BNP concentration using validated commercial ELISA kits. When transferred for biosensor testing, individual aliquots were warmed in ambient to

room temperature before being pipetted manually onto the sensors. Each aliquot was then immediately returned to the freezer, keeping careful track of freeze-thaw cycles in order to minimize sample degradation.

4.3 Single Sample Tests

4.3.1 Spiked PBS Samples

8 artificially graded concentrations of BNP in healthy human serum were tested on the devices to explore the range of device response. Serum was derived from human plasma by spin separating the hemoglobin with a centrifuge at 2000 rpm for 2 minutes, and then separated into 7 aliquots of differing BNP concentration. Trace amounts of hemoglobin have negligible effects on conductivity [36, 37] Up to 0.25 V, the current response was linear, at which point separation began to become more significant (Fig. 10). This serves as confirmation of the well-known fact that increased BNP concentration corresponds directly with greater total accumulation of protein charge, creating a higher gate voltage [38]. By this point, all samples had differentiated according to their respective concentrations in near logarithmic spacing. This demonstrated that the devices were able to successfully respond to samples according to their concentration and served as validation that the biosensors could support the required range of BNP containing the low/high threshold concentration.

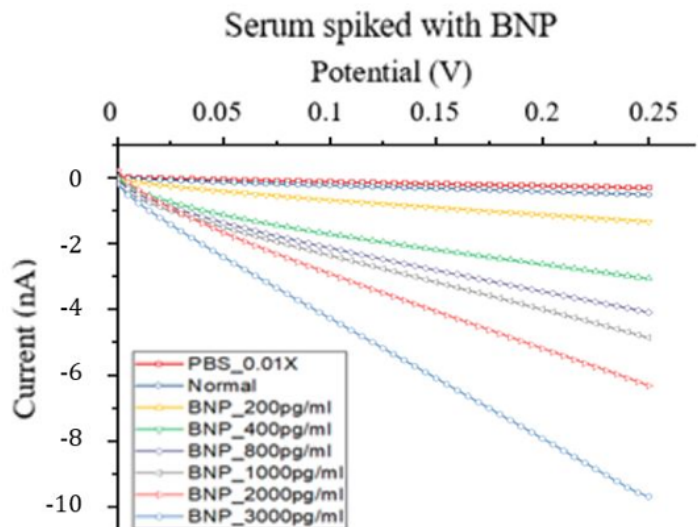


Figure 10: Current response results from spike testing experiment for PBS, control sample, 200, 400, 800, 1000, 2000, and 3000 pg/mL. Linearly increasing current responses demonstrate proper function of the biosensor. Gate voltage is -0.4V due to p-type nature of PANI and prior testing

Samples with higher BNP concentrations were able to bond more fully with the anti-BNP adhered onto the PANI bridge. Doing so creates a buildup of negative charge onto functionalized the PANI substrate, which induces a slight positive alteration to the gate voltage, hence allowing more current to flow through the device. This experiment was conducted to confirm the average concentration of BNP in serum derived from a healthy patient’s blood. It had a slightly higher response than non-conductive 0.01X PBS, as there was little BNP contained in the sample. However, when spiked with increasingly higher concentrations of BNP, the current response increased immediately, confirming that the bonded BNP was altering the gate voltage to allow a greater current response. Broadly, this result gives strong indication that the biosensor framework can be expanded for further antigen-detection-based risk assessment with the modification of different antibodies.

4.3.2 UPMC Patient Serum (Healthy)

Relatively little research has been conducted using human blood or serum with conductometric biosensors, so working with UPMC provided an excellent opportunity to establish baselines. 10 aliquots of serum were drawn from each of 10 healthy subjects and tested to provide a reference current response and check for device testing repeatability. These aliquots were tested across 10 devices and superimposed onto a single graph to show a visual average current response. The current responses develop a heat map with the dark regions showing denser sampling responses (Fig. 11). From the graph, the average current at $0.4 V_{gate} = 0.3 \text{ nA}$ and a total range of 1 nA . Each voltage sweep resulted in a linear current response, which suggests that a chemical stability between PANI-receptors and BNP has been achieved.

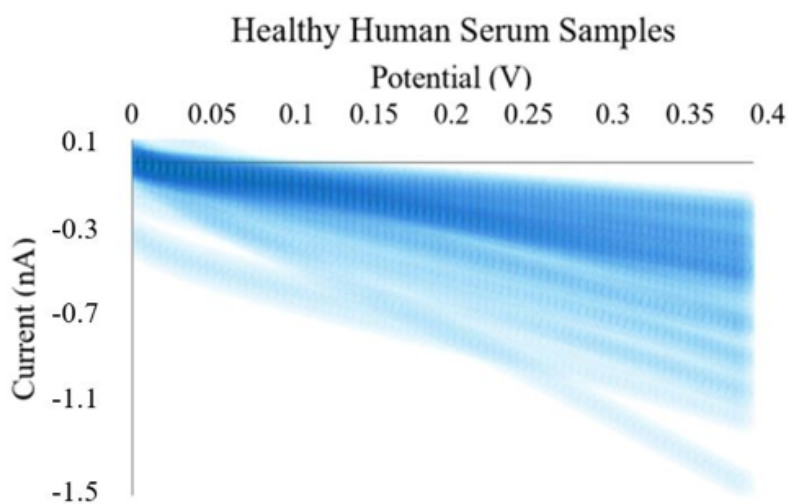


Figure 11: Current responses for 100 baseline (healthy patient blood samples) tests across 10 samples. Each test has 80 points taken during a linear sweep from $[0 - 0.4] \text{ V}$. Results are plotted to form a heatmap – darker regions indicated higher density of results among multiple samples and lighter regions indicate more sparse measurements

Across the 80 total tests, variance was less than 1 nA , with even tighter ranges within each device (Fig. 12). The max variance of measurements in each device was 0.8 nA , and the variance across all samples was 0.93 nA . These results suggest good repeatability within

and across each device. These results were consistent with expectations and showed that the devices were compatible with human serum samples. As expected, the healthy samples yielded a current response on the pico-amp regime, with some outliers breaching 1 nA by the end of the voltage sweep.

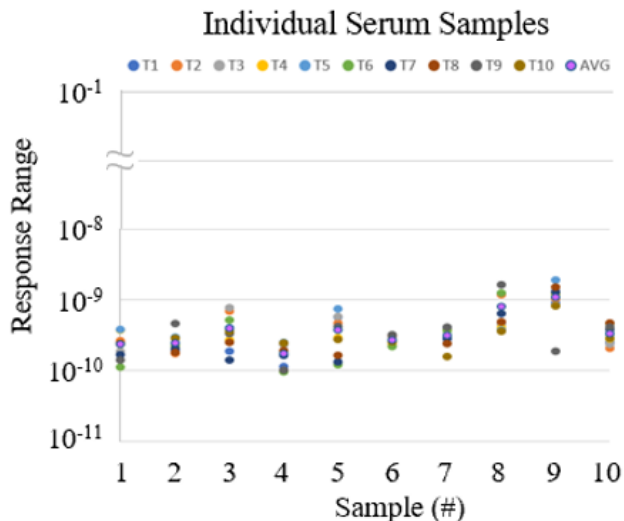


Figure 12: Variance plot organized according to devices that each measurement was taken from. Data characterizes range of current responses of healthy samples. Maximum intra-device range was 1 nA, indicating good replicability and reliability to not in higher ranges

4.3.3 UPMC Patient Serum (Unhealthy)

Next, patient serum samples with measurable BNP were selected for testing. The samples came in five different concentrations of BNP defined in this study: healthy 1 (control 1), healthy 2 (control 2), 600 pg/mL, 800 pg/mL, and 1800 pg/mL. These concentrations were meant to represent two groups: not at-risk (healthy 1, healthy 2, and 600 pg/mL) and at-risk (800 pg/mL and 1800 pg/mL), with a total of 42 trials for each group. The input readings are color coded according to concentration (Fig. 13). Visually, the samples started to differentiate similarly to the spike test (Fig. 10). Strong separation was evident, clearly distinguishing each sample by 0.4 V application. Variance between samples increased with

higher concentrations as expected and resulted in overlap between several samples, especially with 800 pg/mL trials. Additionally, the current magnitude seems to saturate with increased BNP, a characteristic that could be modulated with an increase of anti-BNP concentration during surface modification or change of PANI sheet dimensions. In all cases, healthy samples displayed minimal response, as expected.

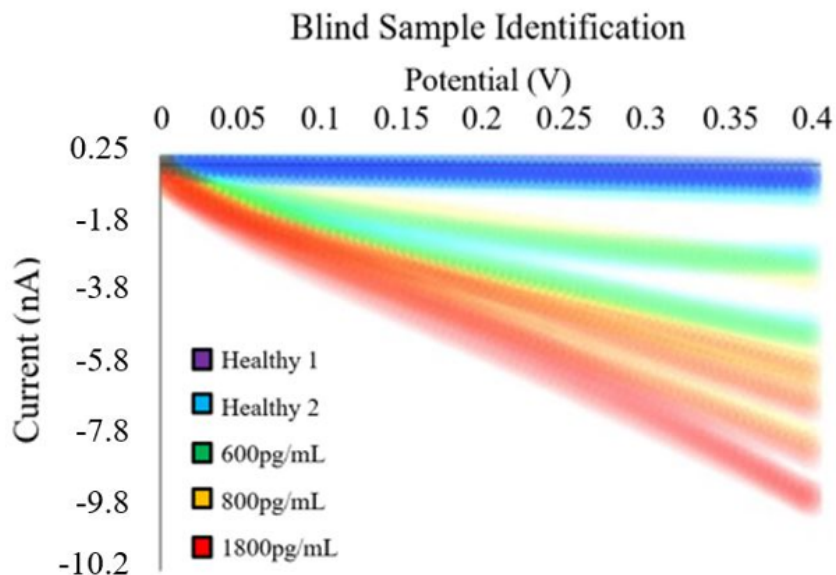


Figure 13: Blind test current responses were color coded according to concentration (control 1, control 2, 600, 800, and 1800 pg/mL). and confusion matrix. Results show clear separation between healthy patients and those with high levels of BNP in blood. As BNP concentration was increased, variance increased significantly at higher gate voltage. Clear separation was achieved between blood samples with trace amounts of BNP and patients with at-risk levels of BNP

4.3.4 Hemolysis Impact

A noted difference between the artificial samples and patient samples is the the presence of unwanted contaminants. Though careful steps were taken to minimize them, there would always be trace biomarkers left, most significantly hemoglobin ion by count. Therefore the

effect of hemolysis on conductivity was explored. Hemolysis is the break down of red blood cells and will inevitably occur sample processing. When broken down, red blood cells will break down into both insulating hemoglobin (HGb) molecules and conducting iron-based ions. Sensitivity tests were conducted on different solutions of HGb:PBS ratios in order to measure the effect of hemolyzed blood cells and determined if there were any major effect on the patient sample conductivity as a result (Fig. 14).

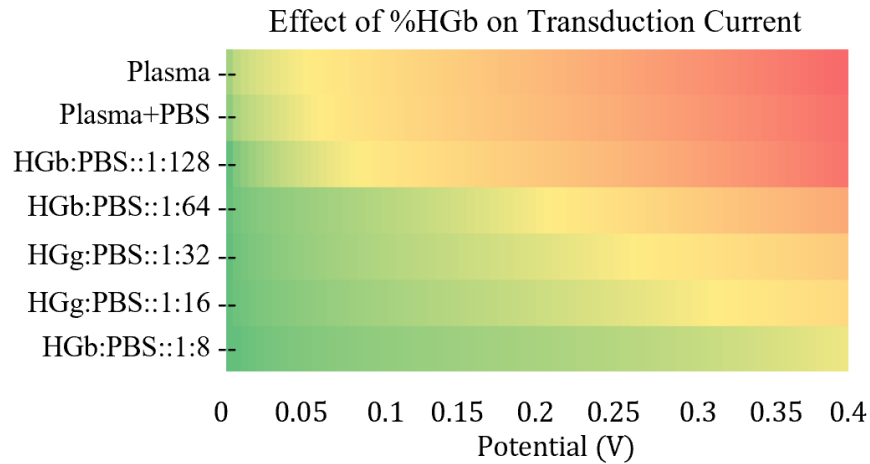


Figure 14: Heat map plot of hemolysis current magnitude sweeps. Green corresponds to lower response, and red corresponds to higher response. The total range in testing is 4 pA, indicating that while there is an inverse relation between hemoglobin concentration and conductivity, the overall effect is quite minimal

Results show that compared to dilution, hemolysis in standard blood processing may be negligible. All measurements were near identical, displaying only a 4 pA difference from the highest concentration of HGb (849 pA) to the lowest concentration (853 pA). Any added conductivity of free Fe^+ ions seems to be counterbalance by solvation due to HGb molecules. Saturation thresholds occur in ranges HGb:PBS :: 1:64-128 and HGb:PBS :: 1:16-8, though this difference too is negligible. The smooth color gradient indicates the HGb concentrations' effect is slightly larger than noise levels itself, however small.

4.4 Multi Sample Tests

4.4.1 Continuous Spiking

6 blood serum aliquots from different UPMC patients with varying BNP concentration samples were applied successively in 30-second intervals, cumulatively increasing the current response of the sensor. This resulted in a step response with increasing magnitude produced by the sensor over a 2.5-minute period (Fig. 15). The antibody-antigen reaction time can be observed as taking several seconds after the application of a higher graded sample. As sampling rate was low in order to accommodate for longer trials, the transitions appear to be abrupt. However, closer inspection shows a more gradual levelling, indicating that the binding occurs at relatively high speed. This confirms expectation from existing literature on antigen-antibody interaction speeds.

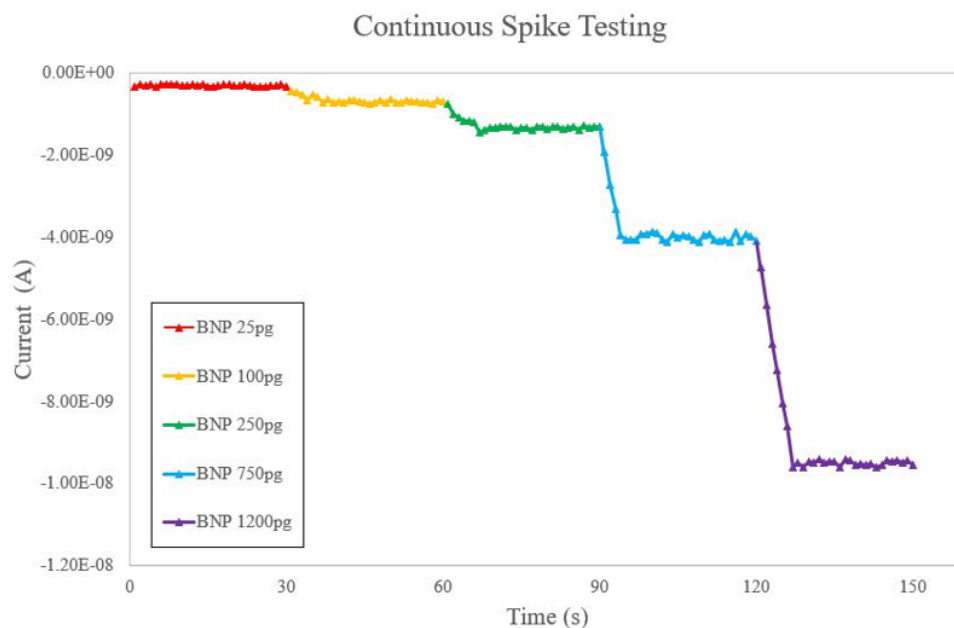


Figure 15: Concentration dependency of increasing levels of BNP (25, 100, 250, 750, 1200 pg/mL). For each application, current magnitude increases in agreement with prior characterization. Bulk reactions take several seconds to reach equilibrium, and appear to occur at a linear rate due to low sampling rate

As theorized, samples with higher BNP concentration produced a higher current response due to an increased immobilization of charged BNP molecules via antibody-antigen interactions. This accumulation of negative charge induces a positive charge over the PANI surface, increasing the conductivity of the p-type semiconducting material, and allowing increased carrier flow. Notably, the effect of adding samples successively was not cumulative, as the saturation current of each concentration matched closely with the peak current of corresponding samples when tested individually. This has an interesting implication that the devices biosensors also have a degree of reusability.

A limit test was conducted by applying a sample with 3500 pg/mL to the sample and ran until the device burned out. Over several trials, compliance current ranged from [13 - 17] nA over a period from [6 - 7] minutes, with rapid decay. The compliance current for a fixed voltage was heavily dependent on PANI bridge sizing and antibody concentration during surface modification. 2.5 μL of a 1:49 antibody-crosslinker solution (2 ng/mL antibody solute) was distributed across the entirety of a 3.5 μm^2 functionalized area. Further testing can be done to observe the effects of different PANI topologies on sensitivity and specificity metrics. Ranges in compliance current and label destruction were likely due to small variances in production of the sensors.

4.4.2 Biomarker Specificity

System specificity was tested in a similar fashion. Two sequences of different solutions of biomarkers were applied to the sensor and the output measured and observed. The first sequence consisted of BNP, followed by myoglobin, creatine-kinase, and c-troponin in natural amounts, before ending with another higher concentration application of BNP (Fig. 16). The result showed strong specificity for BNP over other cardiovascular biomarkers. While each marker did correlate positively with magnitude of current response (~ 0.5 nA), the effect was largely negligible compared to that of BNP, which had approximately 6x the response for every 600 pg/mL added. Specifically, this test confirms that the sensor was able to capture how quickly the sensors responded to the BNP compared to the others. The small observable effect of the other biomarkers is therefore likely due to physical binding on the

device rather than any chemical binding with the antibodies. An additional investigation would be needed to determine the effect of settling time on the current responses of each biomarker, but within the 30 s window, BNP far out responded the others.

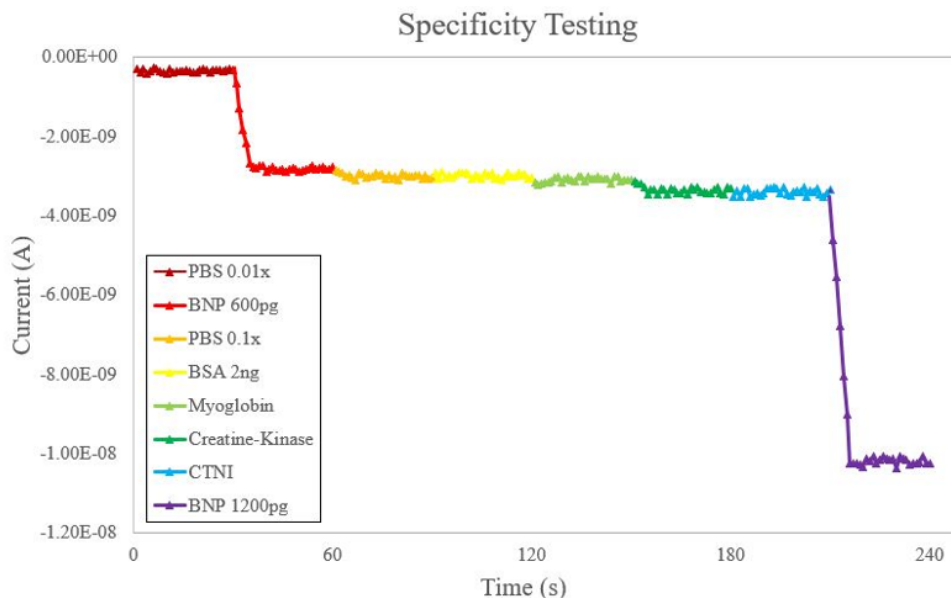


Figure 16: Specificity towards target BNP vs non-target biomarkers. Application of each nontarget biomarker affects current response with less than 10% of BNP sensitivity. The final BNP sample confirms proper sensor function

4.4.3 Reaction Reversability

The second sequence included the addition of a PBS washing step in between each marker. The primary motive for this test was to further investigate why the binding seemed non-reversible under conditions of the previous test. Ordinarily, antigen-antibody interactions are governed by the law of mass action, the principle that describes the equilibria concentrations of a reaction. A corollary is each of those reactions is reversible. However, the results suggest that the antiBNP-BNP interaction is somewhat non-reversible (Fig. 17), as the washing procedure did not greatly overcome the Van der Waals forces of the complex. Although it is a well-known fact that BNP has a high affinity [39, 40], the stability of the

signal throughout the washing (pipette reapplications) is significant and shows high promise for the robustness of the sensor. As with the previous sequence, additional settling time testing would be required to extend results to larger time frames. However, the overall effect of the washing was in lines with expectations. There was a signal destabilization at each application (time points 20, 50, 80, and 110 s) that allowed for clearer observation of the strength of effect of the other biomarkers. Additionally, when compared with prior testing, the 1200 pg/mL sample resulted in a $\sim 10\%$ drop in current response, from 9 nA down to 7.5 nA. Such a result indicates that some portion of the conformed sites were reversed due to the PBS, and it also strengthened the previous hypothesis that the majority of non-targets were physically bound and therefore easily washed away by the PBS.

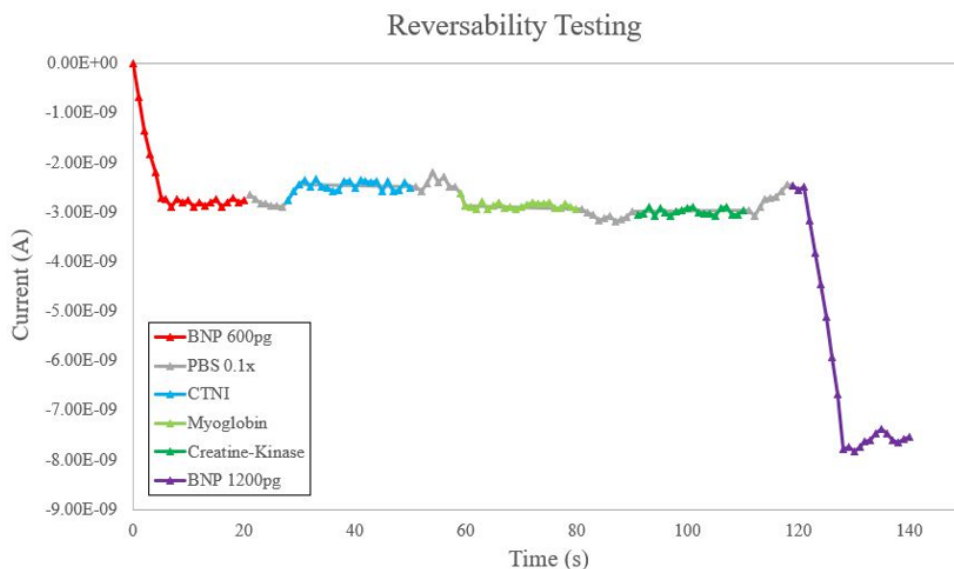


Figure 17: Specificity test with additional intermediate PBS0.1x washing steps to gauge reaction affinities. Washing procedure consisted of 3 rounds of PBS dilution and removal through pipetting. Results indicate that most non target biomarkers are physically bound to the PANI layer, but the BNP antigen-antibody complex is not washed away during the purging, showing high affinity relative to blocked biomarkers

5.0 Determination Methods

5.1 Digital Determination - Machine Learning Analysis

Today, there are many different options for data processing, such as analysis of variance (ANOVA) which determines difference between groups due to interrelational variance, and mechanistic analysis which breaks data sets into input-output relationships. However, these are all causal analyses that only help to explain data. One of the major challenges in current biosensor research is the reproducible data. While most researches have demonstrated excellent sensing performance, there is a general lack of data stability due to large variability in individual devices. Regular monitoring for early diagnosis requires the incorporation of a method like Machine Learning (ML), which has strong causal power as well as a strong predictive power, in order to improve data stability, testing repeatability, and results classification accuracy. ML is a type of artificial intelligence which can be used to increase confidence of results by using adaptive classification algorithms. Currently ML is being implemented in many different fields and research due to its high analytic capability – it has proven to be especially useful in image classification, navigation, and big data visualization. ML may also play a key role in the biosensors scene, because biosensor results are analyzed over long periods of time and can accumulate large histories quickly. Lab results only give insight into one specific instant in the patient’s life, but biosensors are powerful because they can monitor and analyze samples much more often. ML is necessary in order to take advantage of this time frame to identify both current status as well as future trends in the patient’s health [41]. Significant amounts of work has been done to implement ML algorithms into biosensors, including a wrist sensor for seizure detection [42] and glucose-oxidase sensor for predictive monitoring [43]. For cardiovascular biosensors, BNP concentration in the blood can translate directly to an individual’s risk of developing HF. Using ML to find patterns in daily readings can allow for predictions of future health status [44, 45]. This greatly increases a biosensor’s use for early diagnostics and will help realize the concept of lab-on-a-chip (LOC).

5.1.1 Discriminant Analysis

A single-layer neural network was coded in Python to separate sample trials into two categories, healthy or unhealthy. Healthy samples served as the control, while unhealthy was defined according to the outside edge of the gray area, that is any concentration $[C] > 1000$ pg/mL, and unhealthy is labelled as anything below. The neural network first used linear discriminant analysis (LDA) to classify samples. LDA is a statistical method key for preprocessing data for pattern-classification by reducing degrees of freedom. Doing so helps avoid overfitting, which happens when the ML algorithm incorporates noise deterministically into the model. With 30 training samples for each, healthy and unhealthy, the dependent variable of a rough formula for BNP concentration was made in terms of the statistical mean and variation of the electrical measurements – i.e. BNP concentration was expressed as two linear combinations of independent features. Intra and inter-class scatter matrices, S_W and S_B respectively, were calculated according to standard Fisher LDA algorithms to characterize the variance of the training data. Features were then extracted from the resultant covariance matrix through eigen decomposition and separated according to minimal error function by minimization of S_W and maximization of S_B :

$$S_W = \sum_{classes} [\sum_{class} (A_{class} - \mu_{class})(A_{class} - \mu_{class})^T] \quad (5.1)$$

$$S_B = \sum_{class} (\mu_{class} - \mu)(\mu_{class} - \mu)^T \quad (5.2)$$

$$\Sigma_{WB} = S_W^{-1} S_B \quad (pseudoinverse) \quad (5.3)$$

When electrical measurements were taken from new samples, the data set's statistical output was input into the ML predictive model to predict which group the data came from. Test data was sorted to whichever linear combination had a stronger correlation, hence classifying a sample test as either healthy or unhealthy. In order to extend the capability of the ML algorithm and create more robust results, a second assessment method was conducted through quadratic discriminant analysis. QDA is a more robust variation of LDA. It assumes that the covariance matrices are not identical between each variable. This is accomplished by computing quadratic terms in addition to linear terms, leading to a more thorough set of

measurement vectors before determining linear combinations to fit the data into. Doing so gives one extra degree of freedom for the model and with it higher statistical power.

The QDA classification results of the unhealthy patient data (Fig. 13) are presented as a confusion matrix (Fig. 18). Reading the matrix horizontally first tells the rate of actual success – the first row displays that 41 out of 42 unhealthy samples were correctly predicted and the second row shows that 39 out of 42 controls were correctly identified. Reading vertically analyzes the statistical power of the model – the first column tells the α (type 1) error and the second column gives the β (type 2) error. Green highlighted squares indicate desired results, while red indicates misclassifications. After two generations of training, the algorithm was able to achieve an overall accuracy (95.2%), sensitivity (97.6%), specificity (92.9%), precision (93%), and recall (98%). Therefore, the current algorithm with the given sample set has an F-score of 0.95 indicating high power and efficacy.

2nd Generation Network Separation

		Prediction		Total
		Positive	Negative	
Actual	Positive	True Positive 41 48.8%	False Negative 1 1.2%	97.6% 2.4%
	Negative	False Positive 3 3.6%	True Negative 39 46.4%	92.9% 7.1%
Total		93.2% 6.8%	97.5% 2.5%	Success: 95.2% Failure: 4.8%

Figure 18: Confusion matrix of classifier results were used to calculate power and error. All results were comparable to standard methods such as PCA. Metrics derived from the matrix are: accuracy (95.2%), sensitivity (97.6%), specificity (92.9%), precision (93%), and recall (98%)

5.1.2 Principal Component Analysis

A secondary analysis of the results was performed using principal component analysis (PCA) for a reference to compare results using similar methods. Methods followed are widely available in existing literature [46 – 49]. The code was programmed in MATLAB 2015b for both feature extraction of the IV curves and PCA analysis. No constraints were applied and only the first three components were taken. All samples were plotted against three statistical properties as a separated 3-d plot (Fig. 19).

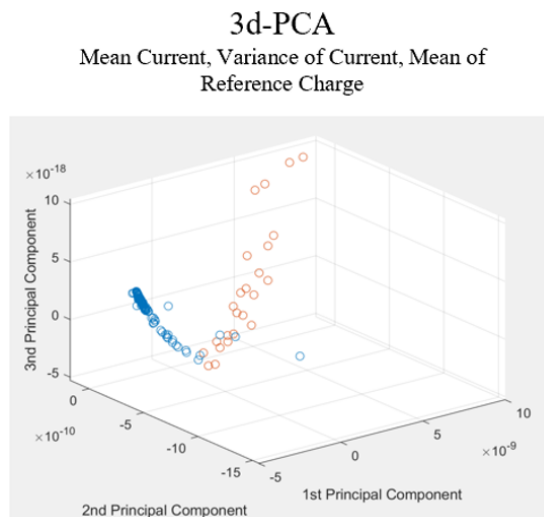


Figure 19: 3d-PCA analysis of blind test samples. Components were mean current, current variance, and mean charge. Blue indicates samples classified as healthy and orange indicates samples classified as unhealthy

The components were the mean of the current response, variance of the current response, and mean of the reference charge respectively. As a result, there are two clear groups of clustering with small overlap. The blue grouping were points all classified as healthy samples, and the orange points were classified as high BNP at-risk samples. The analysis was able to identify 28/30 targets 99/100 non-targets correctly, which also gives an F-score of 0.95, indicating similar power. Therefore, the ML algorithm is comparable in statistical power to PCA, which is a benchmark for separation classifiers.

5.2 Analog Determination - Readout Circuit

5.2.1 Circuit Operation

The circuit has three main stages: 1. Signal-voltage transimpedance amplification, 2. Low-noise logic amplification, and 3. optical readout with LED (Fig. 20). Sequentially, the biosensor output is connected to stage 1, where the nanoampere signal is converted to a microvolt range. Then, the signal is simplified via low noise, ground-tie operational amplifiers up to small logic level. The gain of the system is tuned precisely so that samples of 500 pg/mL BNP concentration will exceed the LED threshold voltage V_t , thereby creating a trinary determination system, LED_{off} for typical levels of BNP and LED_{dim} for potentially concerning levels of BNP, and LED_{bright} for predetermined high levels of BNP. The system was built specifically to develop a powerful yet light-weight circuit that did not require onboard digital processing.

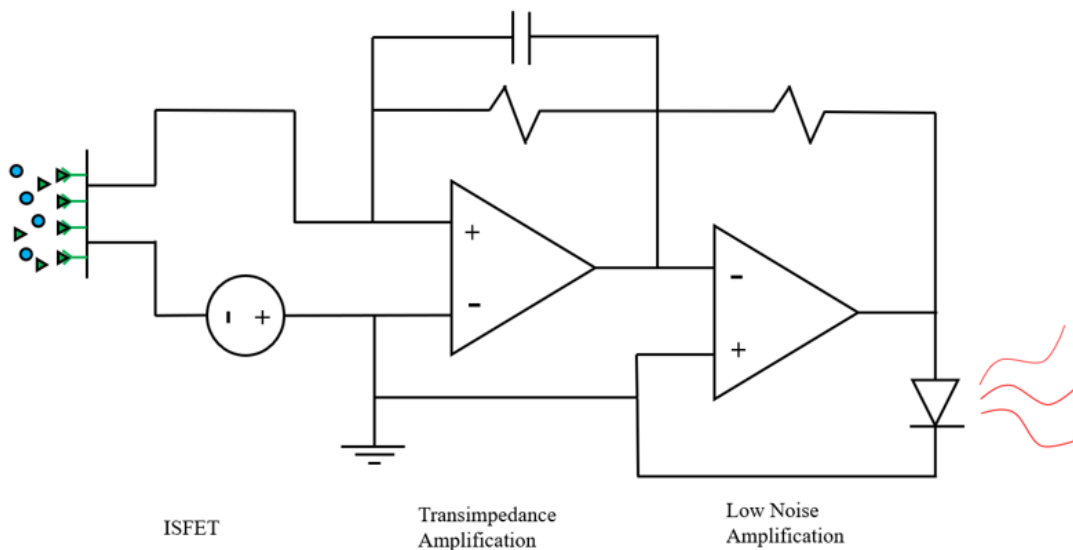


Figure 20: High level block schematic of system. 3 stages are: 1. Current generation through antigen sensing, 2. Transimpedance amplification for voltage control, and 3. Final voltage inversion and amplification

5.2.2 Noise Reduction

One of the largest challenges with the circuit was optimizing noise reduction, which was especially important due to regular single digit nanoampere measurements. For this, a PCB with a common ground plane was used, and any active components were ultra-low noise. The AD8428 chip is a low noise instrumentation amplifier with a gain of 2000 and stable temperature sensitivity and wide bandwidth. It has a $1.3 \text{ nV}/\sqrt{\text{Hz}}$ at 1 kHz and an outstanding 40 nVpp noise from 0.1-10 Hz, making the chipset ideal for low range, high sensitivity applications. Another major feature of the chipset is custom filtering available on each amplifier, which allows for a number of system level modifications. One creative way is by daisy-chaining multiple AD8428 filters together [50, 51]. The method works by making use of the fact that the $1.3 \text{ nV}/\sqrt{\text{Hz}}$ inherent noise is uncorrelated between devices, while input noise is positively correlated, thus causing a $\sqrt{2}$ factor reduction with each additional instrumentation amplifier chained.

5.2.3 Optical Output States

The continuous spike test presented in section 4.4.1 was done while connected to an amplifier readout circuit, and corresponding voltage measurements were taken. The goal was to utilize an LED threshold voltage as a switch powered directly a biosensors output signal. Such a method, rather than directly modulating a transistor switch, allows for a small a pseudo-binary signal. Rather than two states, this enables a third state by introducing a ramp up to full voltage. In terms of diagnostics, this is useful in separating determinations into healthy, caution, and at-risk categories. The states are defined: State 0 – LED_{off} , State 1 – LED_{dim} , State 2 – LED_{bright} . (Fig. 21). The system was able to accurately reflect the sensor output for both the sensitivity and specificity tests, as LED voltage and state was measured concurrently with the BNP sensitivity test.

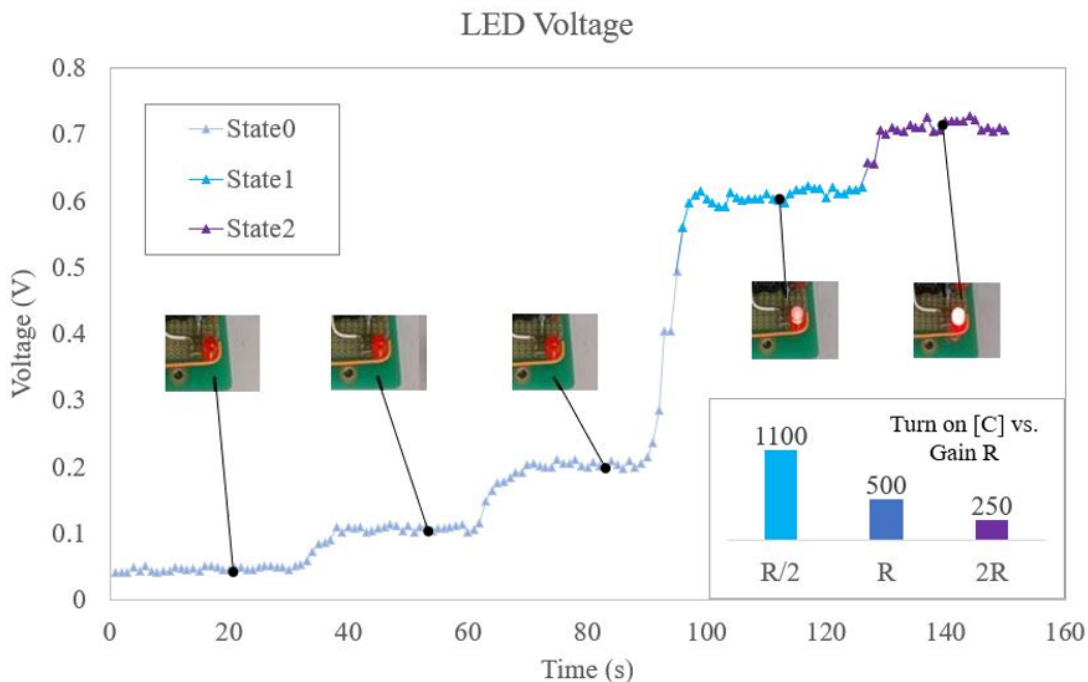


Figure 21: LED states with corresponding visuals. Concentrations applied in order were: 25, 100, 250 (State 0 – LED_{off}), 750 (State 1 – LED_{dim}), and 1200 pg/mL (State 2 – LED_{bright}). Gain was tuned for concentration threshold of 500 pg/mL between State 0 and State 1

With a standard threshold voltage $V_t = 0.65V$, system gain was tuned such that $V_{LED} > V_t$ at 3 nA corresponding to 500 pg/mL. Accordingly, the left three LED states (25, 100, and 250 pg/mL, respectively) are in State 0. After enough antigen has bound to the antibodies when the 600 pg/mL sample is added, the output voltage exceeds the threshold voltage and the LED is able to conduct and enter State 1, lighting up but not at full brightness. Finally, as after the 1200 pg/mL sample is added, the LED reaches saturation voltage and emits maximum brightness, Stage 2. Samples within a 100 pg/mL range of the concentration threshold were unable to be consistently read correctly, and sometimes resulted in flickering. This may be the result of noise introduced by the circuitry, though many efforts were taken to maximize signal to noise ratio. However, a triage use case of this device calls for low resolution and as such the circuit performs satisfactorily.

By simply tuning the gain of the third stage, the concentration at which the LED initially turns on can be controlled nearly linearly. When the half feedback resistance is used, the threshold concentration doubles to 1100 pg/mL. Likewise, when the gain is halved, only half of the base BNP concentration (250 pg/mL) is required to light the LED. This is a functionality that takes advantage of the direct link between LED state and BNP concentration as opposed to encoding the signal through different logic gates.

Similar readings were taken during the specificity test. Initially the LED was in State 0 before application of a 750 pg/mL sample after which the LED is in State 1. Subsequent washing with PBS and adding other biomarkers has negligible affect on LED brightness, while adding a final 1200 pg/mL BNP sample fully pushes the LED from State 1 to State 2, as expected. This is a promising result as it confirms that non-specific binding has a very minor effect on the final output of the system.

5.2.4 System V-I Characterization

Because the transfer function of the system is tuned for linear gain, the overall characteristic expected is that of the limiting component, the LED (Fig. 22). Despite lower readings due to internal impedances, the measured data matches closely with the expected system characteristic. Though a longer current sweep would help establish a more accurate relationship, the tested range is enough to capture a large portion of patient BNP levels. Additionally, this presents a reliable method for both interpolation and extrapolation of bloodstream BNP concentration from LED voltage, building upon sensor current characterizations in previous work.

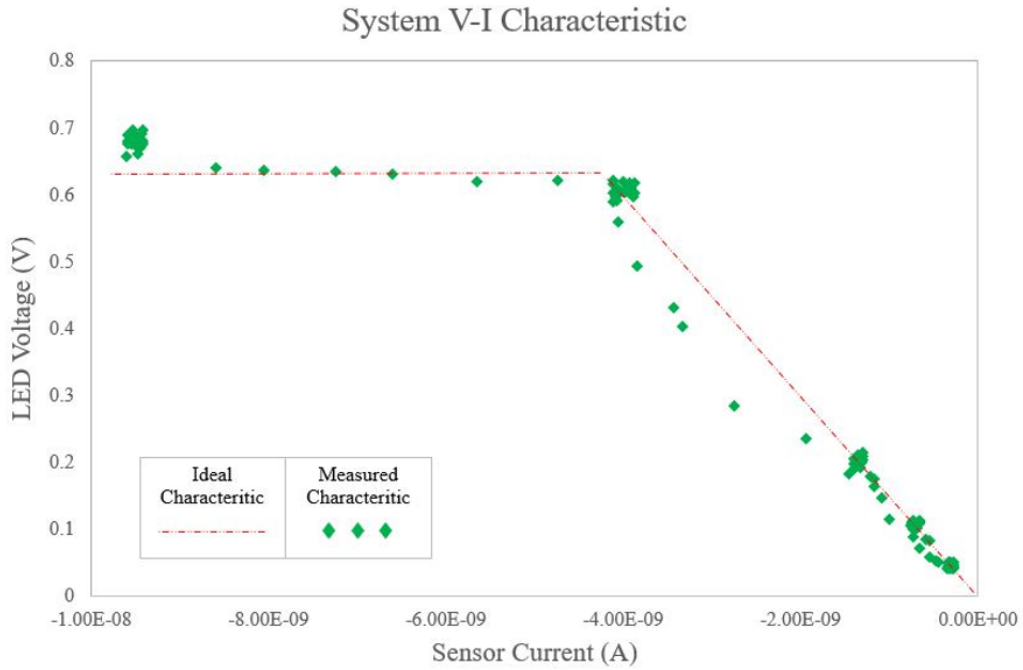


Figure 22: V-I characteristic of system mirrors that of LED, formed by plotting induced sensor current versus output LED voltage. ISFET generates a negative current but the signal voltage is inverted during amplification, resulting in a reflected. Additionally, note that in this circuit operation, LED voltage is a function of sensor current, opposite of standard I-V characteristic convention. Characterization matches expectations and validates holistic circuit design

6.0 Conclusion


This research has demonstrated a proof-of-concept for a lightweight amplification readout circuit meant for trinary determination. The circuit was able to directly translate nanoampere current signals from a PANI ISFET to logical voltage levels for use with a simple LED for visual indication, testing successfully on a range from 25-1200 pg/mL. Sensitivity error was within 100 pg/mL and proved to be enough resolution for the output. The system also displayed good specificity, being negligibly affected by competing protein markers. Results show strong potential in further development of a fully integrated sensor-circuit system.

This research has demonstrated the fabrication and characterization of a new flexible PANI-based biosensor able to sense BNP on pg/mL and ng/mL regime for lab-on-a-chip applications. The sensor is immunoassay-based and functions via conductometry, making it both highly selective and nondestructive. Results suggest compatibility with human serum derived from blood. Spike testing exhibited functionality and signal characterization; baseline testing showed biocompatibility with real human serum samples. Additionally specificity was tested against three other major cardiac biomarkers.

After characterization, two methods of blind sample determination were developed. First, results from blind testing demonstrate a ML algorithm comparable in power to a 3-dimensional PCA, achieving 95% power. This statistical method was able to be used for label prediction and enhance stability of data, indicating strong potential use in diagnostic applications, thereby showing feasibility of the new data assessment method. Second, a proof-of-concept lightweight amplification readout circuit meant for trinary determination. The circuit was able to directly translate nanoampere current signals from a PANI ISFET to logical voltage levels for use with a simple LED for visual indication, testing successfully on a range from [25 - 1200] pg/mL. Sensitivity error was within 100 pg/mL. Results show strong potential in further development of a fully integrated sensor-circuit system.

Appendix B Chipset Data Sheets

1. First page of AD8428 Chip data sheet:



**ANALOG
DEVICES**

**Low Noise, Low Gain Drift, G = 2000
Instrumentation Amplifier**

AD8428

Data Sheet

AD8428

FEATURES

- Fixed gain of 2000
- Access to internal nodes provides flexibility
- Low noise: 1.5 nV/√Hz input voltage noise
- High accuracy dc performance
 - Gain drift: 5 ppm/°C
 - Offset drift: 0.3 μV/°C
 - Gain accuracy: 0.05%
 - CMRR: 140 dB min
- Excellent ac specifications
 - Bandwidth: 3.5 MHz
 - Slew rate: 40 V/μs
- Power supply range: ±4 V to ±18 V
- 8-lead SOIC package
- ESD protection: 5000 V (HBM)
- Temperature range for specified performance: -40°C to +85°C
- Operational up to 125°C

APPLICATIONS

- Sensor interface
- Medical instrumentation
- Patient monitoring

FUNCTIONAL BLOCK DIAGRAM

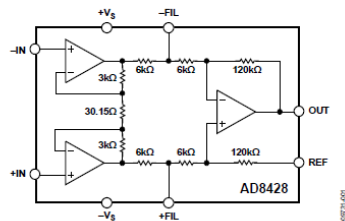


Figure 1.

Table 1. Instrumentation Amplifiers by Category¹

General-Purpose	Zero Drift	Military Grade	Low Power	Low Noise
AD8220	AD8231	AD620	AD627	AD8428
AD8221	AD8290	AD621	AD623	AD8429
AD8222	AD8293	AD524	AD8235	
AD8224	AD8553	AD526	AD8236	
AD8228	AD8556	AD624	AD8426	
AD8295	AD8557		AD8226	
			AD8227	
			AD8420	

¹ See www.analog.com for the latest instrumentation amplifiers.

GENERAL DESCRIPTION

The AD8428 is an ultralow noise instrumentation amplifier designed to accurately measure tiny, high speed signals. It delivers industry-leading gain accuracy, noise, and bandwidth. All gain setting resistors for the AD8428 are internal to the part and are precisely matched. Care is taken in both the chip pinout and layout. This results in excellent gain drift and quick settling to the final gain value after the part is powered on. The high CMRR of the AD8428 prevents unwanted signals from corrupting the signal of interest. The pinout of the AD8428 is designed to avoid parasitic capacitance mismatches that can degrade CMRR at high frequencies.

The AD8428 is one of the fastest instrumentation amplifiers available. The circuit architecture is designed for high bandwidth at high gain. The AD8428 uses a current feedback topology for the initial preamplifier gain stage of 200, followed by a difference amplifier stage of 10. This architecture results in a 3.5 MHz bandwidth at a gain of 2000 for an equivalent gain bandwidth product of 7 GHz.

The AD8428 pinout allows access to internal nodes between the first and second stages. This feature can be useful for modifying the frequency response between the two amplification stages, thereby preventing unwanted signals from contaminating the output results.

The performance of the AD8428 is specified over the industrial temperature range of -40°C to +85°C. It is available in an 8-lead plastic SOIC package.

Rev. A
Information furnished by Analog Devices is believed to be accurate and reliable. However, no responsibility is assumed by Analog Devices for its use, nor for any infringements of patents or other rights of third parties that may result from its use. Specifications subject to change without notice. No license is granted by implication or otherwise under any patent or patent rights of Analog Devices. Trademarks and registered trademarks are the property of their respective owners.

One Technology Way, P.O. Box 9106, Norwood, MA 02062-9106, U.S.A.
Tel: 781.329.4700 www.analog.com
Fax: 781.461.3113 ©2011–2012 Analog Devices, Inc. All rights reserved.

Figure 25: AD8484 general description

2. First page of TLE207x Chipset data sheet:

TLE207x, TLE207xA
EXCALIBUR LOW-NOISE HIGH-SPEED
JFET-INPUT OPERATIONAL AMPLIFIERS
SLOS181C – FEBRUARY 1997 – REVISED DECEMBER 2009

- Direct Upgrades to TL05x, TL07x, and TL08x BIFET Operational Amplifiers
- Greater Than 2× Bandwidth (10 MHz) and 3× Slew Rate (45 V/μs) Than TL07x
- Ensured Maximum Noise Floor 17 nV/√Hz
- On-Chip Offset Voltage Trimming for Improved DC Performance
- Wider Supply Rails Increase Dynamic Signal Range to ±19 V

description


The TLE207x series of JFET-input operational amplifiers more than double the bandwidth and triple the slew rate of the TL07x and TL08x families of BIFET operational amplifiers. Texas Instruments Excalibur process yields a typical noise floor of 11.6 nV/√Hz, 17-nV/√Hz ensured maximum, offering immediate improvement in noise-sensitive circuits designed using the TL07x. The TLE207x also has wider supply voltage rails, increasing the dynamic signal range for BIFET circuits to ±19 V. On-chip zener trimming of offset voltage yields precision grades for greater accuracy in dc-coupled applications. The TLE207x are pin-compatible with lower performance BIFET operational amplifiers for ease in improving performance in existing designs.

BIFET operational amplifiers offer the inherently higher input impedance of the JFET-input transistors, without sacrificing the output drive associated with bipolar amplifiers. This makes them better suited for interfacing with high-impedance sensors or very low-level ac signals. They also feature inherently better ac response than bipolar or CMOS devices having comparable power consumption.

The TLE207x family of BIFET amplifiers are Texas Instruments highest performance BIFETs, with tighter input offset voltage and ensured maximum noise specifications. Designers requiring less stringent specifications but seeking the improved ac characteristics of the TLE207x should consider the TLE208x operational amplifier family.


Because BIFET operational amplifiers are designed for use with dual power supplies, care must be taken to observe common-mode input voltage limits and output swing when operating from a single supply. DC biasing of the input signal is required and loads should be terminated to a virtual ground node at mid-supply. Texas Instruments TLE2426 integrated virtual ground generator is useful when operating BIFET amplifiers from single supplies.

The TLE207x are fully specified at ±15 V and ±5 V. For operation in low-voltage and/or single-supply systems, Texas Instruments LinCMOS families of operational amplifiers (TLC- and TLV-prefix) are recommended. When moving from BIFET to CMOS amplifiers, particular attention should be paid to slew rate and bandwidth requirements and output loading.



Please be aware that an important notice concerning availability, standard warranty, and use in critical applications of Texas Instruments semiconductor products and disclaimers thereto appears at the end of this data sheet.

PRODUCTION DATA Information is current as of publication date. Products conform to specifications per the terms of Texas Instruments standard warranty. Production processing does not necessarily include testing of all parameters.



POST OFFICE BOX 655303 • DALLAS, TEXAS 75265

Copyright © 1997 – 2004, Texas Instruments Incorporated

1

Figure 26: TLE207x general description

Bibliography

- [1] Perera, G. S. et al. Rapid and selective biomarker detection with conductometric sensors. *Small* 17, 2005582 (2021).
- [2] Zhang, X. et al. Affordable automated phenotypic antibiotic susceptibility testing method based on a contactless conductometric sensor. *Sci. Rep.* 10, 21216 (2020).
- [3] Jin, W. & Maduraiveeran, G. Nanomaterial-based environmental sensing platforms using state-of-the-art electroanalytical strategies. *J. Anal. Sci. Technol.* 9, 18 (2018).
- [4] Cesewski, E. & Johnson B. N. Electrochemical biosensors for pathogen detection. *Biosens.* 159, 112214 (2020).
- [5] Kolahchi N. et al. Direct detection of phenol using a new bacterial strain-based conductometric biosensor. *J. Environ. Chem. Eng.* 6, 478-484 (2018).
- [6] Braiek, M. et al. A conductometric creatinine biosensor prepared through contact printing of polyvinyl alcohol/polyethyleneimine based enzymatic membrane. *Microelectron. Eng.* 187-188, 43-49 (2018).
- [7] Huber, S. et al. Multichannel digital heteronuclear magnetic resonance biosensor. *Biosens.* 126, 240-248 (2019).
- [8] Petrellis, N., Spathis, C., Georgakopoulou, K., & Birbas, A. Capacitive Sensor Read-out Circuit for Organic Substance Analysis. *Procedia Tech.* 8, 13-18 (2013).
- [9] Nguyen, T. C., Schwartz, M., Vu, X. T., Blinn, J. & Ingebrandt, S. Handheld readout system for field-effect transistor biosensor arrays for label-free detection of biomolecules. *Phys. Status Solidi A* 212, 1313-1319 (2015).
- [10] Naresh, V. & Lee, N. A review on biosensors and recent development of nanostructured materials-enabled biosensors. *Sensors* 21, 1109 (2021).
- [11] Si, P., Chen, L., Yu, L., & Zhao, B. Dual colorimetric and conductometric responses of silver-decorated polypyrrole nanowires for sensing organic solvents of varied polarities. *ACS Appl. Mater. Interfaces* 10, 29227–29232 (2018).

- [12] Jakhar, S. & Pundir, C. S. Preparation, characterization and application of urease nanoparticles for construction of an improved potentiometric urea biosensor. *Biosens.* 100, 242-250 (2018).
- [13] Rajapaksha, R. D. A. A., Hashim, U., Gopinath, S. C. B., Parmin, N. A., & Fernando, C. A. Nanoparticles in electrochemical bioanalytical analysis. *Nanoparticles in Analytical and Medical Devices* 83-112 (2021).
- [14] S., Soldatkin, O. O., Kucherenko, D. Yu., Soldatkina, O. V., Dzyadevych, S. V. Advances in nanomaterial application in enzyme-based electrochemical biosensors: a review. *Nanoscale Adv.* 1, 4560-4577 (2019).
- [15] Shetti, N. P., Bukkitgar, S. D., Reddy, K. R., Reddy, Ch. V., Aminabhavi, T. M. Nanostructured titanium oxide hybrids-based electrochemical biosensors for health-care applications. *Colloids Surf. B: Biointerfaces* 178, 385-394 (2019).
- [16] Virani, S. S. et al. Heart Disease and Stroke Statistics—2020 Update: A Report From the American Heart Association. *Circulation* 141, e139-e596 (2020).
- [17] Read, S. H. Wild, S. H. Prevention of premature cardiovascular death worldwide. *Lancet* 395, 758-760 (2020).
- [18] Cao, B. et al. Benchmarking life expectancy and cancer mortality: global comparison with cardiovascular disease 1981-2010. *BMJ* 357, j2765 (2017).
- [19] Wolsk, E. et al. Role of b-type natriuretic peptide and n-terminal prohormone BNP as predictors of cardiovascular morbidity and mortality in patients with a recent coronary event and type 2 diabetes mellitus. *J. Am. Heart Assoc.* 116, e004743 (2017).
- [20] Cao, Z., Jia, Y., Zhu, B. BNP and NY-proBNP as diagnostic biomarkers for cardiac dysfunction in both clinical and forensic medicine. *Int. J. Mol. Sci.* 20, 1820 (2019).
- [21] Patterson, C. C. et al. Troponin and BNP are markers for subsequent non-ischaemic congestive heart failure: the Caerphilly Prospective Study (CaPS). *Open Heart* 5, e000692 (2018).
- [22] Zhu, J. et al. A highly sensitive biosensor based on Au NPs/rGO-PAMAM-Fc nanomaterials for detection of cholesterol. *Int. J. Nanomed.* 14, 834-849 (2019).

- [23] Lee, S. P. et al. Highly flexible, wearable, and disposable cardiac biosensors for remote and ambulatory monitoring. *npj Digital Med.* 1, 2 (2018).
- [24] Shanmugam, N. R., Muthukumar, S., Prasad, S. Ultrasensitive and low-volume point-of-care diagnostics on flexible strips – a study with cardiac troponin biomarkers. *Sci. Rep.* 6, 33423 (2016).
- [25] Boutry, C. M. et al. Biodegradable and flexible arterial-pulse sensor for the wireless monitoring of blood flow. *Nat. Biomed. Eng.* 3, 47–57 (2019).
- [26] Meng, K. et al. Flexible weaving constructed self-powered pressure sensor enabling continuous diagnosis of cardiovascular disease and measurement of cuffless blood pressure. *Adv. Funct. Mater.* 29, 1806388 (2019).
- [27] Kaisti, M. et al. Wearable pressure sensor array for health monitoring. *CinC*, 1-4 (2017).
- [28] Sekine, T. et al. Fully printed wearable vital sensor for human pulse rate monitoring using ferroelectric polymer. *Sci. Rep.* 8, 4442 (2018).
- [29] Hwang, E., Seo, J., & Kim, Y. A polymer-based flexible tactile sensor for both normal and shear load detections and its application for robotics. *J. Microelectromech. Syst.* 6, 556-563 (2007).
- [30] Melzer, M. et al. Wearable magnetic field sensors for flexible electronics. *Adv. Mater.* 27, 1274-1280 (2015).
- [31] Rim, Y. et al. Recent progress in materials and devices toward printable and flexible sensors. *Adv. Mater.* 28, 4415-4440 (2016).
- [32] Ha, M., Lim, S., & Ko, H. Wearable and flexible sensors for user-interactive health-monitoring devices. *R. Soc. Chem.* 6, 4043-4064 (2018).
- [33] Kudo, H. et al. A flexible and wearable glucose sensor based on functional polymers with Soft-MEMS techniques. *Biosens.* 22, 558-562 (2006).
- [34] Gao, W. et al. Fully integrated wearable sensor arrays for multiplexed in situ perspiration analysis. *Nature* 529, 509-514 (2016).

- [35] Favier, F. et al. Hydrogen sensors and switches from electrodeposited palladium mesowire arrays. *Science* 293, 2227-2231 (2001).
- [36] Hirsch, F. et al. The electrical conductivity of blood: I. Relationship to erythrocyte concentration. *ASH*, 1017-1035 (1950).
- [37] Zhbanov, A. & Yang, S. Effects of aggregation on blood sedimentation and conductivity. *PloS ONE* 10 (2015).
- [38] Kim, D. et al. An extended gate FET-based biosensor integrated with a Si microfluidic channel for detection of protein complexes. *Sens. Actuators, B* 117, 488-494 (2006).
- [39] Bettencourt, P. M. Clinical usefulness of B-type natriuretic peptide measurement: present and future perspectives. *Heart* 91, 1489-1494 (2005).
- [40] Suga, S., et al. Receptor selectivity of natriuretic peptide family, atrial natriuretic peptide, brain natriuretic peptide, and C-type natriuretic peptide. *Endocrinology* 130, 229-239 (1992).
- [41] Ouchi, K. et al. Machine learning to predict, detect, and intervene older adults vulnerable for adverse drug events in the emergency department. *J. Med. Toxicol.* 14, 248-252 (2018).
- [42] Poh, M. Z. et al. Convulsive seizure detection using a wrist-worn electrodermal activity and accelerometry biosensor. *Epilepsia* 53, 93-97 (2012).
- [43] Gonzalez-Navarro, F. F. et al. Glucose oxidase biosensor modeling and predictors optimization by machine learning methods. *Sensors* 16, 1483 (2016).
- [44] Green, E. et al. Machine learning detection of obstructive hypertrophic cardiomyopathy using a wearable biosensor. *Circulation*. 136(1) (2018).
- [45] Rong, Y. et al. Post hoc support vector machine learning for impedimetric biosensors based on weak protein–ligand interactions. *R. Soc. Chem.* 143, 2066-2075 (2018).
- [46] Richman, M.B. Rotation of Principal Components. *Int. J. Climatol.* 6, 293-335 (1986).
- [47] Sneyers, R., Vandiepenbeeck, M., & Vanlierde, R. Principal component analysis of Belgian rainfall. *Theor. Appl. Climatol.* 39, 199-204 (1989).

- [48] Jolliffe, I.T. Principal component analysis: a beginner's guide—I. Introduction and application. *Weather* 45, 375-382 (1990).
- [49] Stewart, S., Ivy, M., & Anslyn, E. The use of principal component analysis and discriminant analysis in differential sensing routines. *R. Soc. Chem.* 43, 70-84 (2014).
- [50] Kitchin, C. & Counts, L. *A Designer's Guide to Instrumentation Amplifiers*. (Analog Devices, Inc., 2006).
- [51] Gerstenhaber, M., Johnson, R., & Hunt, S. No pain, high gain: building a low-noise instrumentation amplifier with nanovolt sensitivity. *Analog Dialogue* 49, 05 (2015).
- [52] So, S. et al. Induced bioresistance via BNP detection for machine learning-based risk assessment. *Biosens.* 175, 112903 (2021).